Cyanobacteria-ferrihydrite aggregates, BIF sedimentation and implications for Archaean-Palaeoproterozoic seawater geochemistry

Y. Li
Department of Earth and Atmospheric Sciences, University of Alberta, Edmonton, Alberta, T6G 2E3, Canada
e-mail: yuhao3@ualberta.ca

B.R. Sutherland
Department of Earth and Atmospheric Sciences, University of Alberta, Edmonton, Alberta, T6G 2E3, Canada
Department of Physics, University of Alberta, Edmonton, Alberta, T6G 2E1, Canada
e-mail: bsuther@ualberta.ca

A.M. Ilin
Department of Geology, Faculty of Science and Technology, University of the Basque Country (UPV/EHU), Barrio Sarriena s/n, 48940 Leioa, Spain
e-mail: andrey.ilin@ehu.eus

M. Schad
Department of Earth and Atmospheric Sciences, University of Alberta, Edmonton, Alberta, T6G 2E3, Canada
e-mail: schad@ualberta.ca

L.J. Robbins
Department of Geology, University of Regina, Regina, Saskatchewan, S4S 0A2, Canada
e-mail: Leslie.Robbins@uregina.ca

A. Kappler
Geomicrobiology, Department of Geosciences, University of Tübingen, Schnarrenbergstraße 94-96, 72076 Tübingen, Germany
Cluster of Excellence EXC 2124, Controlling Microbes to Fight Infection, Tübingen, Germany
e-mail: andreas.kappler@uni-tuebingen.de

I. Yusta
Department of Geology, Faculty of Science and Technology, University of the Basque Country (UPV/EHU), Barrio Sarriena s/n, 48940 Leioa, Spain
e-mail: i.yusta@ehu.eus

J. Sánchez-España
Department of Planetology and Habitability, Centro de Astrobiología (INTA-CSIC), 28850 Torrejón de Ardoz, Madrid, Spain
e-mail: jsanchez@cab.inta-csic.es

G.W. Owttrim
Department of Biological Sciences, University of Alberta, Edmonton, Alberta, T6G 2E9, Canada
e-mail: gowttrim@ualberta.ca

C.L. Dreher
Geomicrobiology, Department of Geosciences, University of Tübingen, Schnarrenbergstraße 94-96, 72076 Tübingen, Germany
e-mail: carolin.dreher@uni-tuebingen.de

A.J.B. Smith
Palaeoproterozoic Mineralisation Research Group, Department of Geology, University of Johannesburg, P.O. Box 524, Auckland Park, 2006, Johannesburg, South Africa
Department of Science and Technology – National Research Foundation Centre of Excellence for Integrated Mineral and Energy Resource Analysis, Department of Geology, University of Johannesburg, P.O. Box 524, Auckland Park, 2006, Johannesburg, South Africa
e-mail: bertuss@uj.ac.za

D.S. Alessi, M.K. Gingras and K.O. Konhauser
Department of Earth and Atmospheric Sciences, University of Alberta, Edmonton, Alberta, T6G 2E3, Canada
e-mail: alessi@ualberta.ca; mgingras@ualberta.ca; kurtk@ualberta.ca

Abstract

Precambrian banded iron formations (BIFs) are iron- and silica-rich (bio)chemical sediments that are widely believed to have been precipitated by microbial oxidation of dissolved Fe(II). The by-product of these metabolisms – insoluble ferric iron – would have settled through the water column, often as aggregates with the cell biomass. While the mineralogy, composition and physical properties of cell-iron mineral aggregates formed by anaerobic Fe(II)-oxidising photoferrotrophic bacteria have been extensively studied, there are limited studies that characterise cyanobacteria-iron mineral aggregates that formed during oxygenic photosynthesis. This gap in knowledge is important because it impacts sedimentation velocities and the Fe(III) to organic carbon (C_{org}) ratios in the marine sediment pile. Here, we used a recently introduced approach to precisely measure the sedimentation velocity of cyanobacteria-ferrihydrite aggregates and the Fe(III):C_{org} ratios of the cyanobacteria-ferrihydrite aggregates over a wide range of pH and initial Fe(II) concentrations under predicted Palaeoproterozoic atmospheric conditions. Our results indicate that it was highly unlikely BIFs formed at pH <7 via chemical oxidation due to the insufficient sedimentation velocity, even at the maximum predicted Fe(II) concentration of 1800 µM with excess oxygen. Instead, large Banded Iron Formation (BIF) deposits, such as those associated with the *ca.* 2.47 Ga Kuruman Formation in South Africa, would only had been deposited at minimum Fe(II) concentrations of 500 µM at pH 7 or 250 µM at pH 8. The Fe:C_{org} ratios in cyanobacteria-ferrihydrite sediments formed during initially anoxic Fe(II) oxidation experiments represent the maximum values under each condition because we specifically extracted samples after all Fe(II) was oxidised. The Fe(III) to organic carbon ratio was consistently below 4, which is also the ratio required for dissimilatory Fe(III) reduction (DIR). This result indicates that biomass in this case was in excess, which contradicts the low organic carbon content seen in most BIFs. Thus, we suggest that biomass was either physically separated from ferrihydrite aggregates during sedimentation under the influence of ocean currents and waves, or it was degraded prior to DIR. The mineralogical and geochemical evidences of both oxide and carbonate facies from the Kuruman Iron Formation (IF) suggest that ferrihydrite was most likely the precursor along with a significant initial organic carbon input, supporting the proposed cyanobacterially-mediated BIF depositional model and experimental results.

Introduction

Superior-type banded iron formations (BIFs) are (bio)chemical sedimentary rocks that are characteristically rich in iron (~20 to 40 wt.% Fe) and silica (~40 to 50 wt.% SiO_2) (Klein 2005). BIFs were deposited throughout the late Archaean and Palaeoproterozoic over vast expanses of the continental shelves. One of the most extensive of these BIFs, such as the Transvaal Supergroup in South Africa, can reach a lateral extent of up to 500 km and a maximum thickness around 750 m (Beukes, 1983). It is widely accepted that the precipitation of BIFs required some degree of marine planktonic activity to oxidise the aqueous Fe(II) in seawater and trigger the flocculation of Fe(III) (oxyhydr)oxides, such as ferrihydrite, $Fe(OH)_3$ (James, 1954; Klein and Beukes, 1989; Konhauser et al., 2002; Beukes and Gutzmer, 2008; Smith and Beukes, 2023); although we note that others have instead assumed that the surface oceans remained anoxic and devoid of planktonic life, leaving ferrous-silicate

greenalite as the Banded Iron Formation (BIF) precursor mineral (e.g., Rasmussen et al., 2021). Based on the presence of organic-rich shales around 2.5 Ga (i.e. the Mount McRae Shale in Western Australia; Anbar et al., 2007) and the almost universal view that the surface oceans were becoming oxygenated prior to the Great Oxidation Event (GOE) that is timed between 2.45 Ga and 2.32 Ga (Bekker et al., 2004; Konhauser et al., 2011; Gumsley et al., 2017; Warke et al., 2020; Poulton et al., 2021), we are guided by the assumption that BIF precursor sediment reflects a marine surface biosphere (see Konhauser et al., 2023). In this regard, three such biological oxidation mechanisms have been proposed (Konhauser et al., 2002, 2017; Schad et al., 2019a): anoxygenic Fe(II)-oxidising photoautotrophy, also known as photoferrotrophy (reaction 1); aerobic chemolithoautotrophy (reaction 2) with O_2 produced by cyanobacteria; and abiotic oxidation with O_2 produced by cyanobacteria (reaction 3).

$$4Fe^{2+} + HCO_3^- + 10H_2O \rightarrow 4Fe(OH)_3 + CH_2O + 7H^+ \quad (1)$$

$$12Fe^{2+} + O_2 + 2CO_2 + 32H_2O \rightarrow 2CH_2O + 12Fe(OH)_3 + 24H^+ \quad (2)$$

$$4Fe^{2+} + O_2 + 10H_2O \rightarrow 4Fe(OH)_3 + 8H^+ \quad (3)$$

It is hypothesised that microbial biomass would have aggregated with ferrihydrite precipitates that then settled through the water column to the seafloor (Swanner, et al., 2015; Martinez et al., 2016). Subsequently, the organic carbon would have undergone fermentation and then anaerobic respiration in both the water column and sediment, with the Fe(III) in ferrihydrite acting as the terminal electron acceptor, a process known as dissimilatory iron reduction (DIR) (reaction 4; Konhauser et al., 2005).

$$CH_2O + 4Fe(OH)_3 \rightarrow 4Fe^{2+} + HCO_3^- + 7OH^- + 3H_2O \quad (4)$$

This hypothesis not only explains the low content of organic carbon in BIFs (<0.5 wt.%; Gole and Klein, 1981), but also the negative carbon isotope ratios that are recorded in early diagenetic Fe(II)–rich carbonates (Perry et al., 1973; Walker, 1984; Baur et al., 1985; Heimann et al., 2010; Craddock and Dauphas, 2011), the small-scale heterogeneity in $\delta^{56}Fe$ values (e.g., Frost et al., 2007; Steinhoefel et al., 2010; Planavsky et al., 2012), and the presence of mixed valence and Fe(II)-bearing minerals in BIFs, such as magnetite (Fe_3O_4) and siderite ($FeCO_3$) (Li et al., 2013; Posth et al., 2013; Köhler et al., 2013; Halama et al., 2016). In sum, there are abundant isotopic and petrographic arguments that point to the remineralisation of organic matter in primary BIF sediment (e.g. Johnson et al., 2003, 2008a, 2008b; Fischer et al., 2009; Pecoits et al., 2009; Johnson et al., 2013).

One of the best examples that demonstrate the ferrihydrite origin as well as the distinct geochemical characteristics of BIFs described above is the Palaeoproterozoic Kuruman Iron Formation (IF) of the Transvaal Supergroup in South Africa. The age of the Kuruman IF is bracketed between 2 486.6 ± 0.34 Ma and 2 464.0 ± 1.3 Ma based on the high-resolution dating of tuff beds at the base and top of the BIF, respectively (Lantink et al., 2019). The Palaeoproterozoic Asbesheuwels Subgroup of the Transvaal Supergroup in the Griqualand West region of the Northern Cape Province is the thickest, best developed IF succession in southern Africa (Smith, 2018) and also hosts its largest iron ore reserves (Smith and Beukes, 2016). It comprises a carbonaceous shale transition (Kleine Naute Shale) at the base into the lower, deeper water Kuruman and the upper, shallower water Griquatown iron formations (Beukes, 1984; Beukes and Gutzmer, 2008; Smith, 2018). The Kuruman IF mostly comprises micritic banded (ferhythmite) to massive (felutite) IF (Figure 1) (Beukes, 1984) and shows limited instances of sedimentary structures in the form of rare, low amplitude ripples, suggesting most of the IF was deposited below the storm wave base. It has an approximate thickness of 120 to 250 m to the east of the Griqualand West region (i.e., close to the towns of Kuruman and Griquatown; Figure 1), thickening to approximately 750 m to the west (i.e., the towns of Prieska and Koegas) (Beukes, 1984; Beukes and Gutzmer, 2008; Smith, 2018). This has been interpreted to represent a transition from shelf (east) to basin facies (west) (Beukes, 1987; Beukes and Gutzmer, 2008; Robbins et al., 2019). The Griquatown IF, in contrast, contains significant granular and conglomeratic IF (Beukes, 1984), suggesting a hydrodynamically more active depositional environment at shallower water levels. The Asbesheuwels Subgroup is conformably underlain by the carbonates of the Neoarchaean Campbellrand Subgroup (Smith, 2018) and sharply overlain by the mixed clastic and chemical sedimentary Palaeoproterozoic Koegas Subgroup (Schröder et al., 2011).

The mineralogy of the Kuruman IFs comprises all three main mineralogical facies for IFs, namely oxide, carbonate, and silicate facies (Klein, 2005; Bekker et al., 2010) (Figures 1 and 2). The oxide facies contains both haematite and magnetite, with magnetite generally being more abundant in unaltered sections (e.g., Beukes, 1980; Oonk et al., 2017). Where significant haematite is preserved in unaltered sections, it typically occurs as fine (<10 to 20 µm), subhedral, randomly orientated, flaky to tabular-shaped grains whereas the magnetite occurs as slightly coarser (~20 to 100 µm), subhedral to anhedral equidimensional grains (Figure 2A). These minerals commonly co-occur with either mixed or in distinct bands in a matrix of cryptocrystalline quartz (i.e., chert). They can occur as isolated grains distributed in the matrix (Figure 2A) but can agglomerate to form close to monomineralic laminae (Figure 2B). The haematite is also more commonly included in the magnetite (Figure 2B). The carbonate facies mostly comprise siderite and ankerite (e.g., Heimann et al., 2010; Siahi et al., 2020; Tsikos et al., 2022). The siderite commonly occurs as fine (<10 to 30 µm), subhedral grains in a quartz matrix (Figure 2C). Ankerite often has a similar texture (Figure 2B), although it can sometimes occur as larger (~50 to 100 µm) crystals that can aggregate together (Figure 2C and D) and can include finer siderite along its cores and rims (Tsikos et al., 2022). Where mixed oxide-carbonate facies occur, haematite and siderite are commonly included in larger ankerite aggregates or grains (Heimann et al., 2010) (Figure 2C and D). The silicate facies comprise fine (~5 µm), needle-shaped greenalite grains randomly orientated in a chert matrix (Figure 2E).

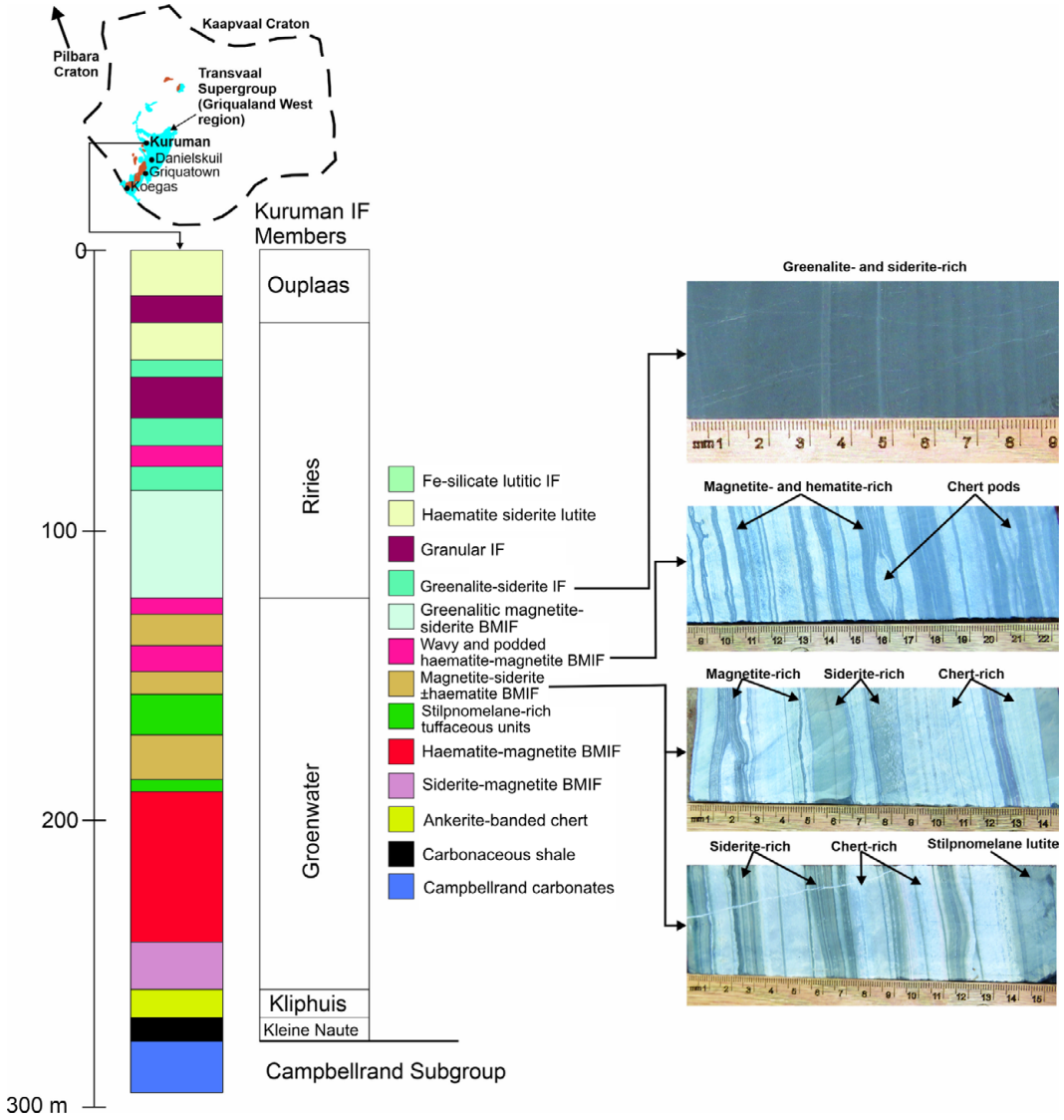

Figure 1. *A lithostratigraphic column of a type section of the Kuruman Iron Formation (IF) as observed close to the town of Kuruman (shelf facies) with core photographs illustrating some of the common lithotypes (adapted from Beukes, 1984; Beukes and Gutzmer, 2008; Robbins et al., 2019). The abbreviation BMIF stands for Banded Micritic Iron Formation.*

The greenalite commonly co-occurs with ankerite, siderite, magnetite, and haematite where the ankerite commonly envelops both the greenalite and oxides (Figure 2E).

The major element composition of the Kuruman IF is dominated by Fe_2O_3 and SiO_2, with generally low Al_2O_3 contents (average 0.11 wt%; Gutzmer et al., 2008). The latter suggests limited clastic input into the depositional system, indicating almost exclusive chemical sedimentary input. The rare earth element characteristics have been shown to be seawater-like, but with positive europium and no cerium anomalies, suggesting that the Kuruman IF is likely a dependable proxy for bulk Palaeoproterozoic ocean chemistry that had significant hydrothermal input and limited oxygenation (Bau and Dulski, 1996). Stable carbon isotopes ($\delta^{13}C_{PDB}$) of carbonates in the Kuruman IF show a range of approximately -9 to -12‰ (Kaufman, 1996; Tsikos et al., 2022). Iron isotopes also cover a range of values from -1.01 to 0.59‰ ($\delta^{56}Fe_{MEAS}$), with magnetite- and haematite-rich samples generally showing more positive and siderite-rich sample showing more negative values (Johnson et al., 2003).

The lithofacies and heterogenous mineralogy of the Kuruman IF can be directly linked to depositional setting, indicating a strong depositional to early diagenetic control on the preserved mineralogy and textures rather than a late secondary replacive control (Robbins et al., 2019). In other words, ferrihydrite was more likely to form the oxide and some parts of carbonate facies in the Kuruman IF, via biological oxidation of Fe(II). In terms of the specific association of cellular biomass and ferrihydrite, most previous studies have focused on photoferrotrophic Fe(II)-oxidising bacteria (Kappler and Newman, 2004; Konhauser et al., 2005; Posth et al., 2013; Schad et al., 2019b; Thompson et al., 2019). From these growth experiments, it is concluded that this particular association

between bacteria cells and ferrihydrite is primarily dependent on the presence of dissolved silica because it has been shown to cause repulsion of ferrihydrite from some photoferrotrophic bacteria cells, resulting in sediments with little organic carbon.

Most recently, Li et al. (2021) showed a strong association of cyanobacteria cells with ferrihydrite, forming cyanobacteria-ferrihydrite aggregates that ranged from sand-sized particles (i.e. mm-scale) up to 2 cm in diameter. If cyanobacteria do indeed facilitate aggregation rather than photoferrotrophs, then it is important to consider how the formation of cell-ferrihydrite aggregates might enhance or diminish the rate and extent of sedimentation. This is significant for two reasons. First, the sedimentation of associated cells will result in the deposition of higher amounts of organic material to the seafloor than cells with weaker associations to ferrihydrite or mineral-free cells that remain primarily suspended in the water column (Konhauser et al., 2005). Second, the sedimentation velocity of cell-mineral aggregates is a crucial parameter to consider when estimating BIF deposition rates. Due to density differences between the average bacterium (1.1 g cm^{-3}; Baldwin et al., 1995) and ferrihydrite (3.8 g cm^{-3}; Posth et al., 2010), fully encrusted cells with a high organic matter content will have a lower density than pure minerals or minerals only loosely associated with cells (Wu et al., 2014; Posth et al., 2010). A slower sedimentation velocity inherently implies that it would take longer for aggregates to travel through the water column, which in turn means that more time is available for degradation of associated biomass during sedimentation from the water column.

To examine the flocculation of cell-mineral aggregates under conditions that better approximate known constraints on Precambrian seawater geochemistry, we conducted sedimentation experiments for cyanobacteria-ferrihydrite aggregates in the presence of 2.2 mM dissolved silica (Maliva et al., 1989; Siever, 1992), a range of initial Fe(II) concentrations from 50 to 1800 µM (Holland, 1984; Tosca et al., 2016; Edmond et al., 1982), and at pH conditions ranging from 6 to 8 to test solubility effects (Grotzinger and Kasting, 1993; Halevy and Bachan, 2017; Krissansen-Totton et al., 2018). Under these conditions, which are thought to reflect the chemistry of Precambrian seawater, we measured the sedimentation velocity of cyanobacteria-ferrihydrite aggregates to facilitate estimations of:

- the amount of Fe(III) that conceivably could have been deposited on an annual basis during BIF deposition, and
- the amount of biomass potentially buried when cyanobacteria were the dominant planktonic organisms driving the deposition of BIFs.

Finally, we examined the experimental results against a suite of geological and geochemical characteristics of the Kuruman IF in South Africa, testing the applicability and feasibility of the proposed depositional model.

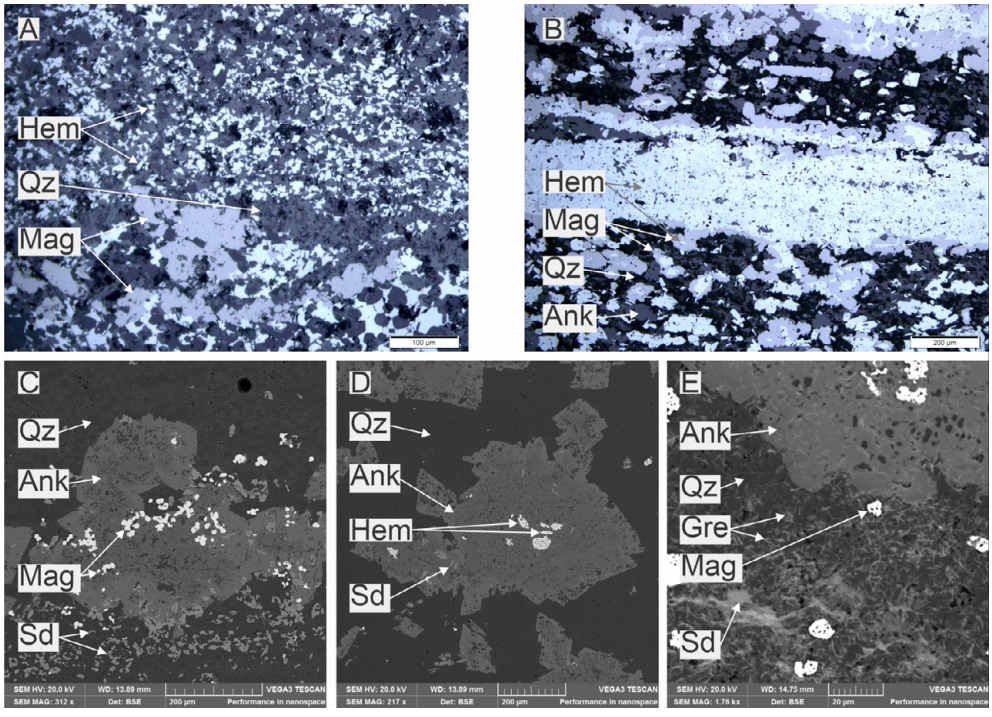

Figure 2. *Reflected light photomicrographs (A) and (B) and scanning electron microscope backscatter images (C) to (E) of drill core samples of the Kuruman Iron Formation (IF), drilled close to Kuruman in the shelf facies, showing the typical appearance of different Banded Iron Formation (BIF) facies. (**A**) Oxide facies showing haematite (Hem) and magnetite (Mag) in a quartz (Qz) matrix. (**B**) Oxide facies showing near a monomineralic Hem band with associated Mag which often includes the Hem and minor ankerite (Ank). (**C**) Carbonate-oxide facies showing finer siderite (Sd) in a quartz matrix and also included in coarser Ank crystal aggregates. Magnetite is also included in the Ank. (**D**) Carbonate-oxide facies showing coarser Ank crystal aggregates containing finer inclusions of Hem and Sd. (**E**) Mixed silicate-carbonate facies showing fine, needle-shaped, randomly orientated greenalite (Gre) in a quartz matric and also included in a larger Ank aggregate.*

Methods

Microorganisms and culturing

The cyanobacterium *Synechococcus* sp. PCC 7002 (referred to hereafter as *Synechococcus*) was chosen to be the representative cyanobacteria in this study. The culture medium and incubation condition of *Synechococcus* followed Li et al. (2021). Cultures were harvested when the optical density (OD_{750nm}) was greater than 0.6. An aliquot of harvested cultures was directly used for open-atmosphere sedimentation experiments; while the rest was then used as an inoculum for initially anoxic growth experiments (see Section reference 2).

Preparation of sedimentation experiments

All experiments were initiated with a mixture of 18.2 MΩ·cm water and NaCl at a concentration of 0.56 M. Depending on the cell density, at least 60 mL of concentrated *Synechococcus* culture was transferred to a translucent acrylic plastic tank with inner dimensions of 20 × 5.1 × 30 cm (length x width x height) at room temperature (~21°C), using a sterile plastic Pasteur pipette. The optical density of the homogeneous mixture was immediately measured to achieve a final OD_{750nm} of 0.15 ± 0.03 after vigorous mixing. Subsequently, an aliquot of a 0.2 M Si stock solution made from sodium metasilicate nonahydrate was added to achieve a final concentration of 2 200 µM. Following this, the pH was adjusted to the target pH values using small additions of concentrated HCl or NaOH as necessary. Then, either an aliquot of a 0.5 M MES (2-(N-Morpholino) ethanesulphonic acid) buffer solution that was fixed at pH 6.1 was added to pH 6 experiments for a final concentration of 5 mM, or solid $NaHCO_3$ was added to pH 7 and 8 experiments to a final concentration of 70 mM to buffer the mixture solution at targeted pH values. Finally, experimental solutions were increased to a final volume of 1.25 L with MilliQ water, and the pH adjusted to the initial target value. The initial pH levels were set at 6.2, 7.2 and 8.2 and were observed to decline by 0.2 to 0.4 over the course of the experiments. Immediately before each experiment started, Fe(II) was added in the form of anoxic 0.2 M ferrous chloride solution using sterile syringes to obtain the desired initial Fe(II) concentrations.

Open-atmosphere sedimentation experiments

Although the pH of Archaean to Palaeoproterozoic ocean water is not well constrained, it is generally accepted to have been between 5.7 to 7.0 (Grotzinger and Kasting, 1993; Halevy and Bachan, 2017; Krissansen-Totton et al., 2018). Below pH 7, *Synechococcus*-ferrihydrite aggregates settle out of the tank water column over an extended period of time, typically days to weeks (Li et al., 2021), making it challenging to accurately measure the settling velocity. Nevertheless, the change in total Fe concentration in solution over time can be measured and used to evaluate the deposition rates of BIFs at pH 6, which approximates the lower end of the range expected for the ancient oceans. Two pH 6 experiments were conducted in duplicates at initial Fe(II) concentrations of 50 µM and 1800 µM, respectively. Immediately after the addition of Fe(II) into the tank, the solution was vigorously stirred until homogeneous. The first sample was extracted at the surface once the solution was still. Subsequent samples were extracted at the same height once every 24 hours for 10 days and 15 days for the 50 µM and 1800 µM experiments, respectively. An abiotic control, with an identical solution composition, was performed adjacent to the microbial experiment.

Experiments at pH 7 and pH 8 were performed essentially as described by Sutherland et al. (2015) and Li et al. (2021). The tank used was identical to that described above. A translucent Mylar film was placed at the back of the water tank from the bottom to a height of 10 cm. A halogen light was placed behind the tank to better visualise and film the settling process. A piece of black construction paper was affixed to the back of the water tank 10 cm above the base to block direct light from the source to the camera through the tank where there was no fluid. A Panasonic HDC-HS250 digital camcorder was used to record the settling experiments. Any ambient light interference was blocked by a black cloth that was lightly draped over the entire setup.

The height of the final solution in the tank for each experiment was exactly 10 cm. Video recording started immediately after the addition of Fe(II) solution, which was then followed by intense stirring until the solution became homogeneous. The duration of each video depended on the initial Fe(II) concentration and pH. Each video recording ended when there was no aggregate settling visible to the naked eye. Video recordings were subsequently processed by the production of a time-lapse series that ran 24 times faster than the original recordings.

Initial Fe(II) concentrations for both pH 7 and 8 experiments were 50, 250, 500, 900, 1200, 1500, and 1800 µM. This range of Fe(II) concentrations was selected to cover the range predicted for Archaean-Palaeoproterozoic bulk seawater between 30 and 500 µM (Holland, 1973; Morris 1993), but also encompass the upper estimates of 1800 µM that reflect Fe(II) concentrations proximal to modern deep-sea vents (Edmond et al., 1982).

The settling of aggregates followed different patterns depending upon the pH and concentration of Fe(II). At low pH and concentrations, settling followed what we call a "slow diffusive mechanism", in which settling could not be seen by naked eye, and was instead determined by *in situ* measurements (Figure S1). (Supplementary data files are archived in the South African Journal of Geology repository (https://doi.org/10.25131/sajg.127.0010.sup-mat)). At higher concentrations and pH values, aggregates were found to settle rapidly through convection driven by localised descending plumes (Figure S1). Aggregates settled the fastest when pH was greater than 10 via the so-called 'concentration front mechanism' (for detailed description and calculation, see Li et al., 2021). The analysis of settling in the first two cases was performed through different methodologies, as described below.

Sedimentation velocity measurements for the slow diffusing mechanism (Section reference 1)

Unlike the plume mechanism, the homogeneous settling of sediments via slow diffusion did not result in any significant

changes in light intensity across the water tank over time. Thus, a different method was required to measure sedimentation velocity. Here, the rate of decline of total Fe content (i.e., the combined concentration of both Fe(II) and Fe(III)) in solution was used to approximate the sedimentation velocity. To quantify the Fe deposition rate, solution samples were extracted at 8 cm depth from the tank bottom to track the total Fe concentration change in solution at 20 to 30 min increments for pH 7 and 8 experiments and at one-day increments for pH 6 experiments. Total Fe in each sample over the experiment duration was measured in triplicates using the Ferrozine assay (Stookey, 1970; Hegler et al., 2008). Changes in total Fe concentration over time were then imported into MATLAB® as a numerical matrix. In MATLAB®, we first plotted the difference between the total Fe concentration and the concentration at any given point ($Ø_0$ - $Ø_T$) over time (T), and subsequently fitted a power law to the first four to six points after the first data point, which gave us the power law exponent (P) and a constant (C) appearing in equation (1). The earliest settling time was given by equation (2) when the final concentration in solution became zero. Assuming that the sedimentation media remained homogeneous during the settling process, we then calculated the amount of time (T) required for the aggregates to settle through the 10 cm water column. The mean sedimentation velocity (MSV) was finally calculated as in equation (3) in cm s^{-1}:

$$Ø_T = Ø_0 - CT^P \quad (1)$$

$$\text{when } Ø_T = 0,\ T = (Ø_0 / C)^{1/P} \quad (2)$$

$$MSV = 10 \text{ cm} \div T \quad (3)$$

in which, $Ø_0$ is the initial total Fe concentration in solution, $Ø_T$ is the total Fe concentration at 8 cm height at a given time, $C = 10^{-b}$, b is the intercept of the linear regression fitted to the first four data points of $Ø_0$ - $Ø_T$ over time (T), P is the slope of the linear regression fitted to the first 4 data points of $Ø_0$ - $Ø_T$ over time (T), and T is time.

Sedimentation velocity measurements for the plume mechanism

A descending plume refers to a horizontally localised vertical flow as a result of negative buoyancy (Turner, 1973). Both the mean and the maximum sedimentation velocities were measured for the plume mechanism. The maximum sedimentation velocities of aggregates that descended via plumes were calculated as described in Li et al. (2021). The descending velocity of a single plume formed in each experiment represented the maximum settling rate of the aggregates under that particular chemical condition (pH and initial Fe(II) concentration). The corresponding time-lapse that runs 24 times faster than the original recording was introduced to MATLAB®. The software subsequently extracted a single vertical time slice per frame at the location where the plume initially formed. MATLAB® was then used to stack continuous images of light intensity versus height and assemble a vertical time series. The sedimentation velocity (cm sec^{-1}) was then calculated from the slope of three highlighted lines, delineated by high light intensity, on the vertical time series. The sedimentation velocity calculated here only accounts for the descending speed of a single plume formed during the sedimentation experiment, and thus represents only the maximum sedimentation velocity under each condition.

The mean sedimentation velocity was measured in a similar way but with different vertical time series. In this case, a plot of the horizontally averaged light intensity as a function of height over time was constructed from every frame of the same timelapse video. These plots were then stacked side by side to create a vertical time series. On the vertical time series, three points were selected to measure the sedimentation velocities. One was at the surface of the water when most sediments were deposited (i.e., when the light intensity decreased significantly). The other two points were chosen at the lower part of the water tank when most sediments were deposited with approximately 10% difference in time. Two lines were then constructed to connect the top point with the two bottom points. The sedimentation velocity was calculated from the average slope of two lines under each condition.

Preparation of anoxic Fe(II) oxidation experiments

(Section reference 2)

The Fe:C_{org} ratios of sediments formed at pH 7 and 8 in a low oxygen setting (i.e., anoxic serum bottles) were examined. Atmospheric oxygen before the GOE was a fraction of the modern (<10^{-5} present atmospheric level (PAL); Pavlov and Kasting, 2002). The pCO_2 was estimated to be 0.001% PAL in the Archaean to an upper limit of 0.1% PAL in the early Proterozoic (Planavsky, et al., 2014; Lyons et al., 2014). Thus, it is important to determine the Fe:C_{org} ratios when oxygen levels were as low as in the Archaean. The same modified A+ media was used in the anoxic Fe(II) oxidation experiment.

After autoclaving, the culturing medium was allowed to cool down to 70°C and subsequently purged with N_2 gas in an ice bath such that the media became anoxic. Once the headspace was purged with the same N_2 gas and brought back to room temperature, N_2-purged 7002 culture was gradually added into the media bottle to a final optical density of 0.16 at 750 nm. Afterwards, N_2-purged anoxic 0.2 M sodium metasilicate stock solution was added into the media mixture to a final concentration of 2 200 µM. The media mixture was then pH adjusted to 7 or 8 and subsequently aliquoted into serum bottles with 135 mL of the mixture media. The serum bottles were then crimped and purged with N_2/CO_2 (90/10, *v/v*) gas for two minutes and headspace was exchanged for 30 seconds. Lastly, the anoxic Fe(II) stock solution (0.2 M) was injected into each of serum bottles using a sterile syringe to reach an initial Fe(II) concentration of 50, 500, 900, or 1800 µM. Cultures were incubated on a shaker at 150 rpm, under constant lighting and at 30°C. The oxidation experiments were run in triplicate while abiotic controls were performed in duplicates.

Samples were extracted using sterile syringes at the beginning of the experiment and subsequently once every 24 hours to monitor the progress of Fe(II) oxidation using Ferrozine assays. Settled cell-mineral aggregates were extracted

using 15 mL Pasteur pipettes from the bottom of serum bottles after the complete oxidation of Fe(II). During extraction, some suspended mineral-cell aggregates were also included in the sample. This suspended portion was later corrected by calculating the amount of Fe(III) in suspension versus deposited using Ferrozine assays to ensure the Fe(III):C_{org} ratios calculated reflect the true ratio of deposited aggregates as described in Section reference 3.

Fe measurements

Both total Fe and Fe(II) concentrations were measured using the Ferrozine assay (Stookey, 1970; Hegler et al., 2008) on either a Beckman Coulter DU®520 UV/VIS spectrophotometer with Fisherbrand™ 1.5 mL semi-micro cuvettes; or a BioTek PowerWave XS Microplate Reader with 96-well microplates and an internal software (KC4™). Eight standards for the Ferrozine assay were prepared by adding ferrous ammonium sulphate hexahydrate into 1 M HCl solution, over a range of concentrations from 0 to 1 000 µM. Samples that required Fe(II) measurements were immediately filtered through sterile 0.22 µm sterile syringe filter units with PES Membrane after extraction and subsequently acidified and diluted five or ten times with 1 M HCl solution. Total Fe measurements always started with reducing Fe(III) in a mixture solution of 10% w/v hydroxylamine hydrochloride in 1M HCl for 30 minutes and followed by addition of Ferrozine solution. Concentrations in µM of both total Fe and Fe(II) were extrapolated from the best-fit linear regression trendline between light absorbance at 562 nm and standard Fe concentrations. Each sample was measured in a triplicate.

Total Organic Carbon (TOC) measurements

Each aggregate sample from anoxic Fe(II) oxidation experiments was first washed with MQ water three times to remove salts and dissolved silica in the media, dried in an oven at 30°C, and powdered using an agate mortar and pestle set. Powdered samples were weighted and loaded in open silver capsules, acidified with gradual addition of 50 µL 1 M HCl until no visible bubbles were observed to remove inorganic carbon, oven dried at 70°C, and lastly the capsules were sealed for total organic carbon (TOC) measurements on a Thermal FLASH 2000 Organic Elemental Analyser using a dry combustion method (Schumacher 2002).

Quantification of Fe:C_{org} ratios (Section reference 3)

Stoichiometrically, for every mole of organic carbon produced by oxygenic photosynthetic cyanobacteria, one mole of oxygen would be produced that would in turn oxidise four moles of Fe(II) to form ferrihydrite. This ratio in the primary sediments to BIFs is significant because it determines the fate of Fe(III) minerals and organic carbon during and after diagenesis in BIFs. Here, we calculated the Fe:C_{org} ratios of cell-mineral sediments that settled in the anoxic Fe(II) oxidation experiment using TOC measurements. Importantly, we sampled the solid at the bottom of the serum bottles as soon as all the Fe(II) was oxidised so that we had a 'true' reflection of the amount of Fe(III) and C_{org} deposited during the oxidative stage versus sampling at some time afterwards when the solids at the bottom of the tank would become more diluted with cyanobacterial biomass growing in the water column in the absence of Fe(II).

The TOC measurements report the percentage of organic carbon in the deposited cell-mineral sediments. The percentages of organic carbon were then corrected for the number of suspended cells in the sediment sample. The corrected percentages were converted to weight (g) assuming that there is a total of 100 g of dry sediments and subsequently divided by the molar weight of carbon 12.011 g mol^{-1} to yield the result in moles. The molar number of Fe(III) was first corrected for the 20% of suspended ferrihydrite particles in the final sediment (based on the ratio of suspended Fe(III) over deposited Fe(III) using Ferrozine method); and converted to weight (g); and finally the molar number was yielded by dividing the weight of deposited Fe(III) by Fe molar weight 55.845 g mol^{-1}.

Scanning Electron Microscopy (SEM)

Cyanobacteria-ferrihydrite aggregate samples were collected at the end of settling experiments from the bottom of the water tank with sterile plastic Pasteur pipettes and put into sterile 2 mL Eppendorf tubes. After one hour, most aggregate sediments settled to the bottom and the supernatant was removed. Samples were further divided into two groups. The first group was fixed to examine the association and structures of cell-mineral aggregates using SEM. The second group was left without any fixation to investigate into the mineralogy and morphology of the aggregates.

Fixed samples were stored in a 2% paraformaldehyde and 2.5% glutaraldehyde buffered fixative solution at 4°C for at least 24 hours before being washed three times with 0.1 M phosphate buffer solution, which was made from a mixture of 0.2 M dibasic sodium phosphate solution and monobasic sodium phosphate solution. Samples were processed through a graded ethanol series followed by a graded ethanol-HMDS (Hexamethyldisilazane) series for dehydration (Bray et al., 1993). Samples were centrifuged at 1500 rpm for three minutes after 20 minutes of incubation in each solution. Finally, samples were extracted from a 100% HMDS solution, gently placed onto clean, uncovered SEM stub mounts and left overnight in a fume hood to dry to completion. All samples were mounted on Al pin stubs and sputter coated with carbon and imaged on a Zeiss Sigma 300 VP field emission scanning electron microscope (FESEM) at 10 kV and working distance of 7 mm (SEM laboratory, Department of Earth and Atmospheric Sciences, University of Alberta).

Parallelly, samples were also analysed without a fixation procedure in order to verify the formation of the aggregates in the least Fe-doped experiments and investigate the aggregates' morphology. The precipitates were analysed under FESEM with coupled energy dispersive X-ray spectroscopy (EDX) at SGIker Advanced Research Facilities (the University of the Basque Country / Euskal Herriko Unibertsitatea). Washed samples were pipetted onto double-sided adhesive carbon tape adhered onto a SEM carbon specimen mount (Ted Pella, CA, USA), dried,

subjected to three minutes of plasma cleaning and carbon-coated. Samples were analysed using a JSM-7000F FESEM (JEOL, Japan) coupled with INCA 350 EDX (Oxford Instruments, UK). The EDX was calibrated with the reference Cu foil throughout each session, The microscope was operated in both secondary electron (SE) and backscattered electron (BSE) modes at 20 kV acceleration voltage, 1 nA beam current, 10 mm working distance, vacuum <8.35 x 10^{-4} Pa and 60 seconds acquisition time at every point of chemical analysis of EDX. Raw X-ray intensity values were ZAF corrected using the INCA software (Oxford Instruments, Abingdon, UK) with a set of standards for quantification.

X-ray Diffraction (XRD)

Authigenic ferrihydrite minerals formed in solution are inherently amorphous (Schwertmann and Fisher, 1973) and thus it is challenging to clearly identify them using XRD. However, we still attempted to identify the solid phases formed in our experiments, hoping to complement SEM results. For solid phase identification, selected unfixed samples were washed by adding 1.2 mL MilliQ water, resuspended in an ultrasonic bath, and subsequently centrifuged for one minute at 13.2 rpm (Eppendorf 5415D, Hamburg, Germany). The samples were then transferred onto zero-background silicon plates and analysed on a PANalytical X'Pert Pro diffractometer (Malvern Panalytical Ltd., Almelo, The Netherlands) at SGIker. The diffractograms were acquired in a continuous scan range of 5 to 70° 2θ with the step size of 0.001° (acquisition time of two hours per spectra) and rotating speed of 15 rpm. We used Cu Kα radiation generated at 40 kV, 40 mA, a programmable divergence slit, graphite monochromator and a PIXcel detector. The presence of the monochromator, placed before the detector, was crucial for reducing the impact of the fluorescence. Diffraction data were processed using X'Pert High Score software with the ICDD database.

Results

Sedimentation mechanisms

Depending on initial pH values and Fe(II) concentrations, there were three different sedimentation mechanisms by which cyanobacteria-ferrihydrite aggregates were deposited through the water column (Figure 3). At pH 6, slow diffusion is the only settling mechanism regardless of initial Fe(II) concentration due to slow Fe(II) oxidation. Between pH 7 and 9, aggregates settled either via a plume mechanism at Fe(II) concentrations >900 µM or via slow diffusion when Fe(II) <900 µM. When pH was >9, the predominant mechanism switched to a rapidly descending concentration front, where most aggregates were deposited within the first ten minutes.

Sedimentation velocity at pH 6

Two pH 6 sedimentation experiments (50 µM and 1800 µM), with their corresponding abiotic controls, were conducted to assess the feasibility of the lower end of the predicted range for Archaean-Palaeoproterozoic ocean pH. In all four experiments, cell-ferrihydrite aggregates settled in the form of slow diffusion. Plumes or concentration fronts did not form during these experiments.

The estimated average rates of total Fe decline over time from pH 6 experiments are shown in Table S1. The minimum and maximum time required to deposit all Fe(III) at the bottom of the water tank were 9.29 days (abiotic experiment with 50 µM initial Fe(II)) and 32.23 days (biotic experiment with 50 µM initial Fe(II)), respectively. The corresponding maximum and minimum rates of sedimentation were 1.04 x 10^{-5} ± 1.74 x 10^{-6} cm s^{-1} to 4.38 x 10^{-6} ± 2.47 x 10^{-6} cm s^{-1}. In all cases, the rate of Fe sedimentation was fastest during the first half of the experiment duration and then significantly declined during the second half. At the end of each experiment, a thin veneer of light brown sediment was visible at the bottom of the water tank.

Sedimentation velocity at pH 7

The sedimentation velocities calculated for pH 7 experiments are summarised in Table 1. Amongst the seven experiments conducted at pH 7, sediments were deposited via slow diffusion in four experiments with initial Fe(II) concentrations below 900 µM, while sediments were deposited in the form of plumes in the other three with initial Fe(II) greater than 900 µM. The average sedimentation velocity varied significantly among the seven experiments, ranging from a minimum rate of 7.46 x 10^{-5} ± 1.95 x 10^{-5} cm s^{-1} to a maximum rate of 3.96 x 10^{-3} ± 3.96 x 10^{-4} cm s^{-1}. These correlate well with the initial Fe(II) concentrations in a linear relationship (Figure 4). The average sedimentation velocities in experiments with deposition via plumes are one to two orders of magnitude faster than those with slow diffusion. When sediments settled as plumes, a single plume usually formed first that subsequently initiated a dynamic fluid motion. Immediately afterwards, multiple plumes formed, and the entire body of the sedimentation media started moving across the water tank. The maximum velocity of a descending plume is calculated at 0.036 ± 0.004 cm s^{-1} with 1800 µM initial Fe(II).

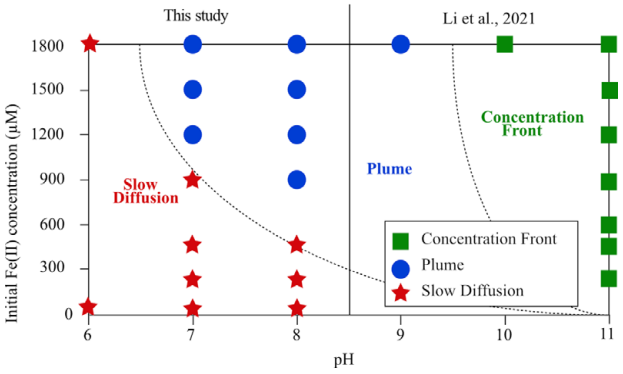

Figure 3. *Phase diagram showing the distribution of three sedimentation mechanisms with respect to initial Fe(II) concentrations and pH (after Li et al., 2021). The dashed lines represent the boundaries between mechanisms. Experiments that are conducted in this study at pH 6, 7 and 8 are separated from previous work.*

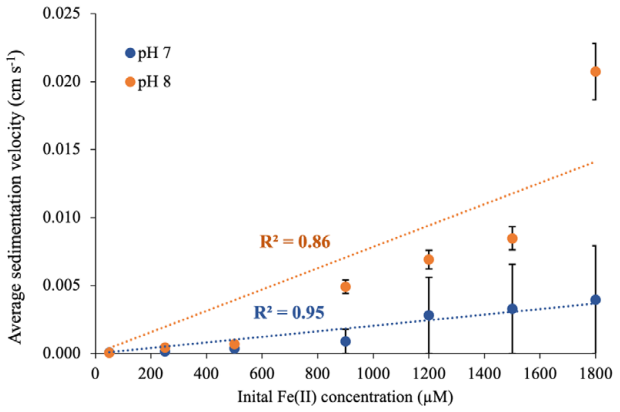

Figure 4. *Linear correlation between sedimentation velocity (cm s^{-1}) and initial Fe(II) concentrations at pH 7 and pH 8. Values are the mean from triplicates ± 1 standard deviation.*

Aggregates slowly grew in size because the initially formed aggregates incorporated more particles during sedimentation. The aggregates could be visually differentiated as they were up to 0.1 cm in diameter. The remaining sedimentation media had a light green color at the end of experiments but appeared to be cloudy because many small aggregates remained in suspension. On the other hand, sediments were deposited more slowly in experiments where slow diffusion was the settling mechanism. Suspended sediments were estimated to be clay to silt sized based on a visual evaluation. We only conducted visual evaluation of aggregate sizes because the aggregates were soft and thus were easily broken into small pieces, and the sizes of the aggregates were constantly changing.

Sedimentation velocity at pH 8

The sedimentation velocity also varied amongst pH 8 experiments (Table 1), ranging from a minimum of 5.08 x 10^{-5} ± 2.47 x 10^{-5} cm s^{-1} to a maximum value of 2.07 x 10^{-2} ± 2.07 x 10^{-3} cm s^{-1}. Similar to pH 7 experiments, sedimentation velocity is linearly related to the initial Fe(II) concentration (Figure 4). It took up to 120 minutes for most of the aggregates to be deposited in experiments where the plume mechanism was observed. During the first 45 minutes to one hour of each experiment, aggregate settling was minimal because it took time for the dissolved Fe(II) that was introduced into the sedimentation media to be gradually oxidised and form ferrihydrite. The first plume usually appeared after a significant number of small aggregates formed *in-situ*, which was evident from the color transition of the sedimentation media from an initial vibrant green to a light green colour (Figure S1). The descending and subsequent ascending fluid motion from the first plume led to multiple localised density contrasts and the corresponding formation of multiple plumes. This series of chain reaction-like motions also caused initially fine-grained individual aggregates to slowly coalesce to reach particle sizes of 0.1 to 0.3 cm in diameter (as determined by direct measurements from snapshots of video recordings). Towards the end of each experiment, these large aggregates started to settle individually while additional plumes formed and dissipated. Finally, a layer of loosely packed aggregates formed at the bottom of the water tank. The sedimentation media became semi-transparent and light green with only a few visible and suspended aggregates. The maximum sedimentation velocity calculated for a single descending plume is 0.074 ± 0.005 cm s^{-1} with 1800 µM Fe(II). Experiments where settling occurred by slow diffusion at pH 8 behaved similarly to their counterparts at pH 7. Sedimentation was homogeneous.

Table 1. Summary table of the average sedimentation velocities measured for pH 6, pH 7 and pH 8 experiments with their sedimentation mechanism.

Initial pH	Fe(II) concentration (µM)	Sedimentation mechanism	Average velocity (cm s^{-1})	Maximum velocity (cm s^{-1})
6	50	Slow diffusion	4.38 x 10^{-6} ± 2.47 x 10^{-6}	N/A
6	1800	Slow diffusion	6.24 x 10^{-6} ± 2.541 x 10^{-6}	N/A
7	50	Slow diffusion	7.46 x 10^{-5} ± 1.95 x 10^{-5}	N/A
7	250	Slow diffusion	1.45 x 10^{-4} ± 4.24 x 10^{-5}	N/A
7	500	Slow diffusion	3.82 x 10^{-4} ± 6.97 x 10^{-5}	N/A
7	900	Slow diffusion	8.84 x 10^{-4} ± 5.13 x 10^{-5}	N/A
7	1200	Plume	2.81 x 10^{-3} ± 2.81 x 10^{-4}	0.035 ± 0.003
7	1500	Plume	3.28 x 10^{-3} ± 3.28 x 10^{-4}	0.034 ± 0.010
7	1800	Plume	3.96 x 10^{-3} ± 3.96 x 10^{-4}	0.036 ± 0.004
8	50	Slow diffusion	5.08 x 10^{-5} ± 2.47 x 10^{-5}	N/A
8	250	Slow diffusion	4.41 x 10^{-4} ± 4.64 x 10^{-5}	N/A
8	500	Slow diffusion	6.93 x 10^{-4} ± 6.21 x 10^{-5}	N/A
8	900	Plume	4.91 x 10^{-3} ± 4.91 x 10^{-4}	0.056 ± 0.005
8	1200	Plume	6.91 x 10^{-3} ± 6.91 x 10^{-4}	0.058 ± 0.008
8	1500	Plume	8.48 x 10^{-3} ± 8.48 x 10^{-4}	0.062 ± 0.010
8	1800	Plume	2.07 x 10^{-2} ± 2.07 x 10^{-3}	0.074 ± 0.005

Effect of cyanobacteria cells on the sedimentation velocity of aggregates

The disparities of measured settling velocities between abiotic control experiments and biotic experiments revealed various effects of cyanobacteria cells on the sedimentation velocities of aggregates that formed under different geochemical conditions. Amongst the nine abiotic control experiments performed at pH 6 to pH 8, all but one experiment showed that the cyanobacteria slowed the sedimentation velocities of settling aggregates; this was inferred from faster decline rates of total Fe concentration in abiotic experiments compared to their biological counterparts (Table S1). There was only one abiotic experiment at pH 6 with 1800 µM initial Fe(II) that showed a slower rate of total Fe decline compared to its corresponding sedimentation experiment with *Synechococcus* cultures.

Fe:Corg ratios in cell-mineral sediments (anoxic Fe(II) oxidation experiments)

After correction for suspended organic carbon and Fe(III) mineral particles (see Section reference 3), the results of Fe:C_{org} ratios of deposited cyanobacteria-ferrihydrite sediments formed in initially anoxic Fe(II) oxidation experiments with four different initial Fe(II) concentrations at both pH 7 and pH 8 are summarised in Table 2. In all 24 cultures, Fe:C_{org} ratios were consistently below the theoretical ratio of 4 (Kappler and Newman, 2004) with a minimum ratio of 0.23 (pH 7; 50 µM initial Fe(II)) and a maximum ratio of 3.64 (pH 8; 1800 µM Fe(II)). There is a consistent positive linear relationship between Fe:C_{org} ratios and initial Fe(II) concentrations at both pH values (Figure 5).

Mineralogy

In all XRD patterns of the samples extracted at the end of the experiment with different initial Fe(II) concentrations, we observed a primary broad diffuse peak with the maximum being between 26.9° 2θ (3.02Å) at pH 7 and 31.8° 2θ (2.81Å) at the pH 8, which are coherent with amorphous silica (Khouchaf et al., 2020). Additionally, the precipitate from the experiment with the initial Fe(II) concentration of 1800 µM and pH 8 showed the presence of two poorly defined diffraction peaks at 34.7° 2θ (2.58Å) and 60.5° 2θ (1.53Å) (Figure 6), consistent with the two-line ferrihydrite (Drits et al., 1993). By contrast, the sample with the same Fe(II) concentration but formed at pH 7 did not show clear diffraction at these angles. It is worth noting that although we were able to identify the respective diffraction peaks of two-line ferrihydrite from diffractograms, it is also apparent that the solid phases are poorly crystalline, which is also a typical character of ferrihydrite. Although other samples did not show definite diffraction peaks of ferrihydrite, subsequent SEM studies confirmed the presence of similar Fe precipitates.

SEM analyses confirmed the formation of Fe precipitates at both pH 7 and 8 in the considered range of initial Fe(II) concentrations (Figure 7A to D). Samples corresponding to experiment done with the lowest 50 µM Fe(II) concentration showed a predominance of silica-rich precipitates over Fe, shifting that ratio towards Fe at higher dissolved Fe(II) concentrations. The common diameter of the aggregates ranged from 100 to 500 nm (Figure 7A; 500 µM Fe(II)) which usually coalesced into bigger aggregates (Figure 7B). With increasing Fe(II) concentrations, the size of both single spherical particles and the complex aggregates tended towards larger diameters (700 to 1 000 nm), and contained a greater amount of mineralised bacterial moulds (Figure 7C). In addition to the common spherical shape, at pH 8 and 1800 µM Fe(II), rosette-like Fe precipitates were found (Figure 7D). Although the HMDS-dried samples showed that even at the highest Fe concentration some bacteria remained free of Fe precipitates, in general most cells were completely entombed by precipitates (Figure 7E). Finally, given that the fixed samples were not sonicated during the SEM preparation, abundant flocculation between bacteria and mineral aggregates was observed, thus increasing the size of a single particle to up to 32 µm (Figure 7F).

Table 2. Summary table of the average Fe(III): C_{org} ratios calculated from cell-mineral sediments that formed in anoxic Fe(II) oxidation experiments at both pH7 and pH 8. Values are mean from triplicates ± 1 standard deviation.

Initial pH	Initial Fe(II) (µM)	Average TOC (wt. %)	Average Fe(III): C_{org} ratio
7	50	40.75 ± 3.77	0.26 ± 0.04
7	500	26.34 ± 2.92	0.52 ± 0.08
7	900	20.35 ± 2.97	0.75 ± 0.17
7	1800	9.10 ± 0.97	2.18 ± 0.34
8	50	23.64 ± 2.51	0.60 ± 0.09
8	500	15.33 ± 2.52	1.11 ± 0.27
8	900	8.59 ± 0.49	2.33 ± 0.19
8	1800	7.10 ± 0.75	3.11 ± 0.46

Discussion

Co-deposition of Synechococcus cells with Fe minerals

Experiments previously conducted with photoferrotrophs have shown that in the presence of dissolved silica, there is only limited cell-mineral aggregate formation (Schad et al., 2019b; Thompson et al., 2019). Consequently, it has been suggested that there should have been very little organic carbon in the sediments during BIF deposition if photoferrotrophs were the sole type of microbial oxidiser of Fe(II). However, in this study, we found compelling evidence of strong association of *Synechococcus* cells with ferrihydrite when grown in the presence of dissolved Si. This relationship between the *Synechococcus* cells and Fe(III) solid phases is indicated by two lines of evidence. First, the apparent transition from an initial vibrant green colour, attributed to the *Synechococcus* cells, to the semi-transparent light green colour of the final supernatant following settling is the direct result of cyanobacterial cells being co-deposited with ferrihydrite during sedimentation. Second,

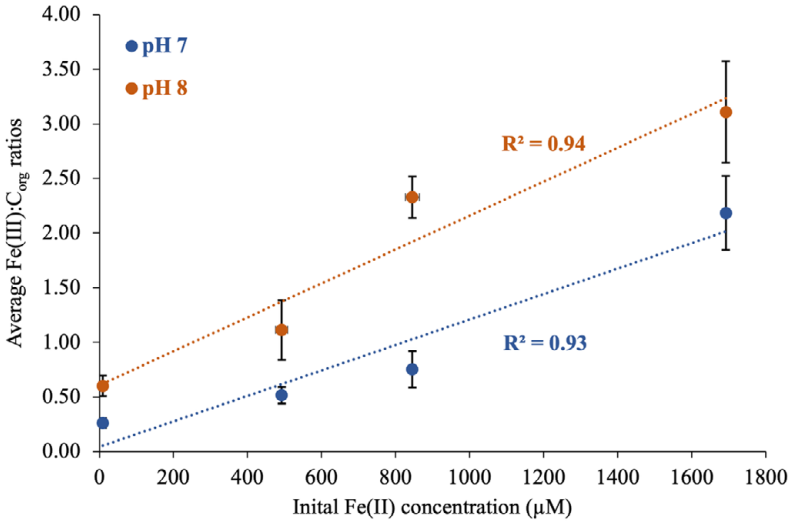

Figure 5. *Linear correlation between average Fe:C_{org} ratios and initial Fe(II) concentrations at pH 7 and pH 8.Values are the mean from triplicates ± 1 standard deviation.*

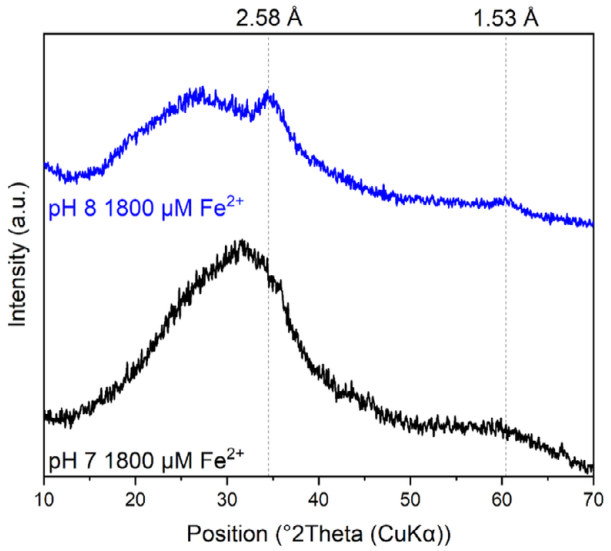

Figure 6. *X-ray diffraction patterns of the precipitates formed in experiments with the highest initial Fe(II) concentration (1800 µM Fe(II)) at both pH 7 and 8. The dotted lines show the position of the main peaks of two-line ferrihydrite consistent with that reported by Drits et al. (1993)*

SEM images of the final sediment confirmed that *Synechococcus* cells were not only co-deposited with ferrihydrite, but some were also partially to fully encrusted with ferrihydrite. Moreover, the soft and voluminous nature of these aggregates also demonstrated that some cyanobacteria cells were entrained within the aggregate structures (Figure 7). An implication of shielded and encrusted organic carbon is that some cyanobacteria remains would have been protected from heterotrophic microorganisms, such as fermenters and DIR, and would have been preserved as biomass during BIF formation (Konhauser et al., 2005). It is well documented that Fe(III) minerals promote preservation of organic matter (Kleber et al., 2005; Lalonde et al., 2012), although the preservation potential and the interactions between biomass and heterotopic bacteria under Archaean-Palaeoproterozoic conditions needs further investigation. Interestingly, the distinct $\delta^{13}C$ signature of the Kuruman IF implies that DIR indeed was essential to fractionate the C-isotope pool. The prerequisite of DIR is sufficient C_{org} input in the sediment pile (i.e. co-deposition of biomass and ferrihydrite).

Nine abiotic control experiments for sedimentation were similarly conducted at pH 6, 7 and 8 as a comparison to the biotic experiments. The flux of Fe removal from the water column was calculated for each experiment with its respective abiotic control as per Section reference 1 (Table S1). In eight cultures (1 at pH 6, 3 at pH 7, and 4 at pH 8), it was determined that *Synechococcus* had a negative effect on the sedimentation velocity, meaning that *Synechococcus* cells slowed the settling of ferrihydrite. This results from the aggregation of ferrihydrite and cells, which, ultimately leads to an increased aggregate volume, but significantly decreases the aggregate density. As such, an overall increase in the buoyancy of the aggregates was observed which promoted slower settling.

Sedimentation mechanism and banded iron formation (BIF)

There is a total of three sedimentation mechanisms reported regarding the deposition of cyanobacteria-ferrihydrite aggregates;

- concentration front (Li et al., 2021),
- plume and
- slow diffusion.

The concentration front mechanism was only observed at pH higher than 9, which is beyond the predicted Archaean-Palaeoproterozoic pH range. In this study, both slow diffusion and plume mechanism were observed under more realistic ancient seawater geochemical conditions. The slow diffusion mechanism resulted in average velocities that are one to three

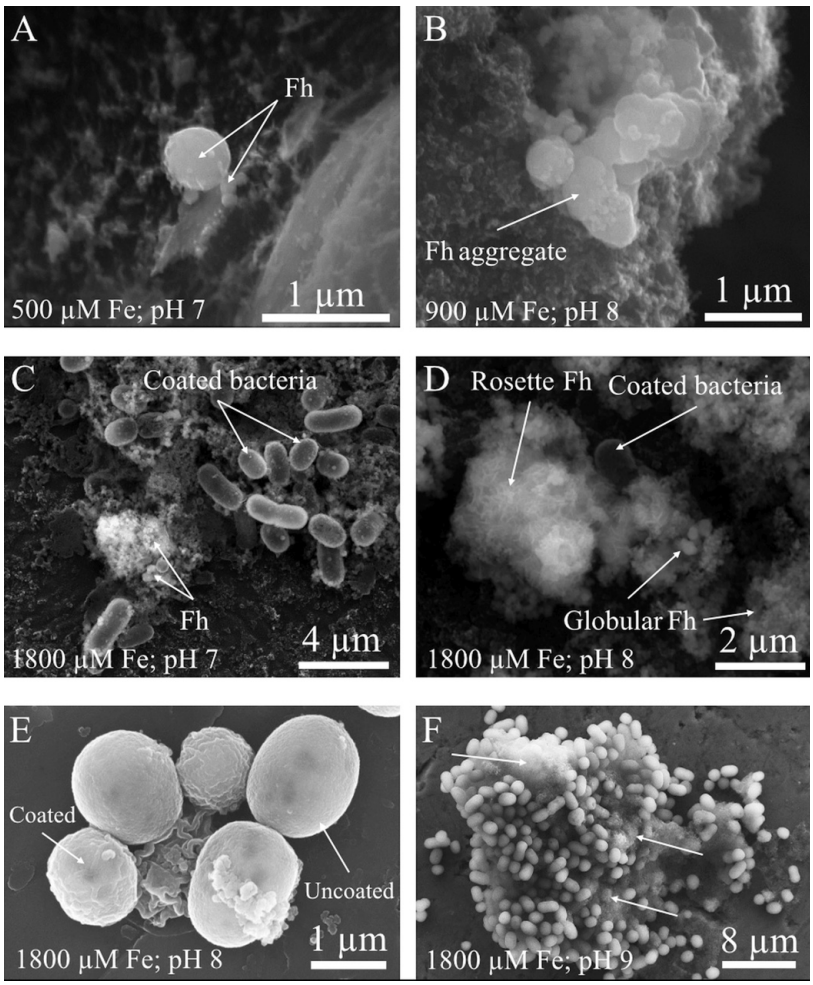

Figure 7. *Scanning Electron Microscopy (SEM) micrographs of the Synechococcus-ferrihydrite aggregates displaying strong association with each other. (**A**) Scarce Fe precipitates detected in the sample with initial 500 µM Fe(II) at pH 7; (**B**) Ferrihydrite aggregates in the sample with 900 µM Fe and pH 8; (**C**) Very abundant Fe precipitates and ferrihydrite-coated bacterial moulds in the sample with 1800 µM Fe at pH 7. (**D**) Different morphology of ferrihydrite precipitate at pH 8 and 1800 µM Fe. (**E**) A close-up of HMDS-dried bacteria showing that the cell surfaces were either covered with ferrihydrite nanoparticles or clean of precipitates even at 1800 µM Fe(II). (**F**) An irregularly-shaped cell-mineral aggregate of approximately 32 µm. White arrows indicate cells that were entrained inside the aggregates.*

orders of magnitude slower than plume mechanism. Aggregates deposited exclusively via slow diffusion at pH 6 regardless of the initial Fe(II) concentration (Table 1). The abiotic Fe(II) oxidation rate at pH 7 is known to be faster than it at pH 6 (Singer and Stumm, 1970; Stumm and Morgan, 2012), therefore, at pH 6, aggregates formed at a slow rate and were sparsely distributed. Importantly the small aggregates formed initially did not coagulate to form larger and heavier particles but instead were only deposited individually.

At pH 7 with a Fe(II) concentration lower than 900 µM, or at pH 8 with an Fe(II) concentration lower than 450 µM, the aggregates formed at a faster rate, but there were not enough aggregates formed to promote particle coagulation, which again resulted in slow diffusion. Thus, slow diffusion should have been the predominate sedimentation mechanism if the Archaean-Palaeoproterozoic ocean was either at pH 6, or at pH 7 and 8 when low concentrations of Fe(II) described above were upwelled onto the continental shelves.

The plume mechanism occurred when larger and heavier coagulated aggregates settled as localised convective cells, which required a high density of initially formed particles in solution: this was observed at higher pH and Fe(II) concentrations. The movement of aggregates increased the chance of aggregate collision and coalescence, promoting faster settling velocities. In a scenario where higher Fe(II) concentrations, greater than 900 µM at pH 7 or greater than 450 µM at pH 8, were brought to continental shelves, the plume mechanism would have replaced slow diffusion and led to short-term but higher sedimentation velocities.

Combining the observations and results from this study and Li et al. (2021), both the initial Fe(II) concentration and pH conditions were the primary controls on the sedimentation mechanism, and subsequently determined the sedimentation velocity. The sizes of aggregates formed via plumes and slow diffusion were drastically different due to the initial Fe(II) concentrations as well as pH. Increasing pH contributes to a

greater degree of deprotonation of surface hydroxyl groups (OH) on ferrihydrite minerals and more extensive aggregation (Dzombak and Morel, 1990), particularly in the 0.56 M NaCl solution used here to mimic seawater ionic strength, which promotes cation bridging among negatively-charged mineral particles. Hence, an elevated initial Fe(II) concentration and pH level would lead to the formation of greater quantities of larger aggregates in a shorter timeframe, ultimately triggering local fluid instabilities that led to the development of plumes. On the other hand, when fewer and smaller aggregates formed over a longer time due to a lower Fe(II) concentration and pH, it was unlikely for them to coagulate but settled as small individual aggregates.

Sedimentation velocity

We note from the outset that extrapolating from small-scale experiments to the open ocean is limited by numerous issues, two being the lack of lateral extent to which the particles could be transported and the absence of currents. Therefore, our laboratory-based experiments are not intended to replicate the intricacies of coastal and shelf settings. Rather they offer an alternative approach to provide fresh perspectives on the deposition of BIFs.

The sedimentation velocity at pH 7 ranged from 7.46×10^{-5} ($\pm 1.95 \times 10^{-5}$) cm sec^{-1} to 0.036 ($\pm$ 0.004) cm sec^{-1}. If the pH of Archaean and Palaeoproterozoic oceans was 7, then 0.036 cm sec^{-1} would represent the maximum settling velocity of cell-ferrihydrite aggregates. Recall that the maximum sedimentation velocity for experiments that settled via the plume mechanism only accounted for the descending rate of a single plume, which means that only a small fraction of aggregates settled at this velocity. The remaining aggregates settled out at a slower rate. Assuming that cyanobacteria-ferrihydrite aggregates formed within the first 100 m of the water column, it would have taken 12.8 days to settle through the remaining 400 m of the entire 500 m water column. This is more than 3.8 days longer than previously estimated by Konhauser et al. (2005) for photoferrotroph-ferrihydrite aggregates based on sedimentation rates estimated from Stokes Law. The sedimentation velocity for experiments at pH 8 ranged from 5.08×10^{-5} ($\pm 2.47 \times 10^{-5}$) cm sec^{-1} at 50 µM Fe(II) to 0.074 ($\pm$ 0.005) cm sec^{-1} at 1800 µM Fe(II). Therefore, for the aggregates to settle through the same 400 m water column it would have taken between 9 113 to 6.25 days, respectively. We acknowledge that the much higher number for settling time has no practical consequence, as particles of this size are influenced by processes not accounted for in Stokes Law, such as Brownian motion and current advection. There was a strong and positive correlation observed between the sedimentation rate and initial Fe(II) concentration at both pH 7 and pH 8 (Figure 4).

Archaean and Palaeoproterozoic ocean pH *(Section reference 4)*

The experiments conducted here allowed us to place some additional constraints on the pH of the Archaean to Palaeoproterozoic oceans coincident with BIF deposition when cyanobacteria were the primary Fe(II) oxidisers. To date, reconstructing ancient seawater pH remains poorly resolved owing to the lack of suitable proxies. In this regard, the overall consensus is that the pH of Archaean-Palaeoproterozoic oceans lies broadly within the range of 6 to 8 (Blättler et al. (2017; Grotzinger and Kasting, 1993; Halevy and Bachan 2017; Krissansen-Totton et al., 2018).

Here we use an entirely different method to estimate ancient seawater pH. Li et al. (2021) measured the sedimentation velocity of ferrihydrite in seawater-like conditions at extremely high dissolved Fe(II) concentrations (1800 µM) and demonstrated a positive correlation with pH. Using a similar approach, but over a much wider range of pH conditions and Fe(II) concentrations, we build on those earlier findings. For instance, at pH 6 the average sedimentation velocity was extremely slow, ranging from 4.38×10^{-6} ($\pm 2.47 \times 10^{-6}$) to 1.04×10^{-5} ($\pm 1.74 \times 10^{-6}$) cm sec^{-1}, depending on Fe(II) concentrations and the presence of cyanobacteria cells. Taking a simplified and conservative approach and assuming aggregates travel vertically through a water column, i.e., without horizontal flow in the absence of currents (which future work will need to consider), and at a steady velocity, the time it would take for Fe(III) mineral aggregates to settle through a 150 m water column to the bottom of a continental shelf would be between 39 637 and 16 693 days. We note that this is not a realistic number, but it serves the purpose of providing a minimum sedimentation velocity because currents would likely further slow the process. For instance, the seawater residence time in modern coastal settings, such as Barnegat Bay in New Jersey and the Mondego Estuary in Portugal, range from as low as one or two days to, in rare circumstances, a maximum of 50 days (Kenov et al., 2012; and Defne and Ganju, 2015). Given the modern seawater residence times, the vast majority of aggregates formed at pH 6 would have been brought beyond continental shelves, and thus resulted in little to no BIF deposition, or more likely ferrihydrite sedimentation in deeper waters that ultimately led to their subduction and loss from the rock record (Keller et al., 2023; Zhang et al., 2023).

It is generally accepted that Fe(II) in the early oceans was sourced from hydrothermal vents with subsequent upwelling to the continental shelf (Holland, 1973; Posth et al., 2013). With a minimum sedimentation time of 16 693 days as projected based on sedimentation velocities derived from our pH 6 experiments, and with or without planktonic cyanobacteria involved, there would not be enough precursor ferrihydrite deposited to form BIF sediment. Instead, most ferrihydrite would have been exported back to deeper ocean through surface currents away from shoreline. Furthermore, if we re-calculate the sedimentation rate for BIFs as in Konhauser et al. (2005) and Kappler et al. (2005) based on changes in total Fe concentrations in solution over time, a sedimentation velocity of 0.000048 mm $year^{-1}$ for 50 µM Fe(II) experiment and 0.0011 mm $year^{-1}$ for 1800 µM Fe(II) is expected, both of which are orders of magnitudes lower than previous BIF sedimentation rate estimated at 0.033 mm $year^{-1}$ (Pickard, 2002). Thus, with confidence, we propose that it is highly unlikely that BIFs were formed in pH 6 oceans given the extremely slow sedimentation velocity expected, which would be insufficient to deposit massive IFs.

However, our observed sedimentation rates would be sufficient to form BIFs at either pH 7 or 8 over a small range of Fe(II) concentrations. Using similar constraints to fulfil a more realistic residence time of aggregates in seawater over continental shelves, the minimum Fe(II) requirement to form BIFs is 1200 µM at pH 7 (61 days) or 900 µM at pH 8 (36 days). Accordingly, we suggest that in order to account for the deposition of large Superior-type BIFs at the Archaean-Palaeoproterozoic boundary at *ca*. 2.5 Ga, seawater pH must have been at least 7. In conjunction with recent isotopic constraints and modelling estimates (Blättler et al., 2017, Halevy and Bachan, 2017; Krissansen-Totton et al., 2018), this would suggest a more constrained pH range of 7.0 to 8.0.

Fe:C_{org} ratios in cell-mineral sediments and excess Fe(III) in primary banded iron formation (BIF) sediments

The theoretical Fe:C_{org} ratio in cyanobacteria-ferrihydrite aggregates is 4 when assuming that all cells are associated with ferrihydrite and no oxygen was consumed by other reactions, which is also the exact same theoretical ratio required to facilitate DIR. On the one hand, to obtain this ratio in the primary BIF sediments, this would have necessitated:

- cyanobacteria-derived oxygen to be the sole oxidant for dissolved Fe(II), and
- all Fe(III) mineral formed as a by-product of oxygenic photosynthesis to be associated with newly produced biomass.

Furthermore, the theoretical Fe(III):C_{org} ratio of 4 for DIR does not include the organic carbon that is required for cell assimilation. Not surprisingly, the Fe:C_{org} ratios yielded from both biological Fe(II) oxidation studies (Posth et al., 2010; this study) and biological Fe(III) reduction studies (Roden and Zachara, 1996; Schad et al., 2022) were all uniformly below 4. In fact, to form Superior-type BIFs, the only prerequisite is that there was an excess amount of Fe(III) in the BIF sediments after DIR, which inherently implies that the Fe:C_{org} ratio in primary BIF sediments due to biological Fe(II) oxidation must be higher than the Fe:C_{org} ratio required for DIR. Due to a significant amount of carbon that is incorporated into biomass, experimental results indicate that the lower limit of Fe:C_{org} ratio for DIR is 2.8 (Roden and Zachara, 1996).

In this study, the anoxic Fe(II) oxidation experiments yielded ratios that were consistently below the theoretical ratio of 4. More precisely, seven out of the eight cultures resulted in a ratio below the lower experimental threshold of 2.8. This result is in a good agreement with similar ratios calculated by Posth et al., (2010) where Fe(II) was oxidised by *Rhodobacter ferrooxidans sp*. strain SW2 during anoxygenic photosynthesis. In order to preserve Fe(III) minerals in BIFs, the Fe:C_{org} ratio must have increased from an initial value of below 2.8 in the cyanobacteria-ferrihydrite aggregates to a ratio that must have exceeded at least 2.8 in the BIF sediments. The change in the Fe:C_{org} ratio could have occurred, for example, due to physical separation of biomass from Fe(III) minerals in the time after the cell-Fe(III) mineral aggregates formed but before magnetite (and siderite) formed during diagenesis (Konhauser et al., 2005). The only experiment with a ratio higher than 2.8 (3.11) was conducted with 1800 µM Fe(II) at pH 8. The difference between the two ratios is the amount of Fe(III) that should theoretically have been preserved following DIR, which is 0.31 mole of Fe(III) or 10% of the Fe(III) originally deposited in the primary sediments. On the contrary, it was estimated that around 20 to 30% of the original Fe(III) was preserved in BIF deposits (Konhauser et al., 2005; Schad et al., 2022). The difference in the extent of Fe(III) preservation indicates that even when the Fe:C_{org} ratio in the primary BIF sediments was formed under the most favourable geochemical conditions, i.e., ones that exceeded the ratio required for DIR, a mechanism to separate C_{org} from Fe(III) was still needed to achieve a minimum extent of 20% Fe(III) preservation to ultimately form BIFs.

Many hypotheses have been proposed to explain the possible mechanisms that lead to biomass separation. For instance, Konhauser et al. (2005) proposed three mechanisms that are relevant here. First, if solely anoxygenic photosynthetic bacteria generated the Fe(III), then excess Fe(III) in the sediments could have occurred if there was a non-quantitative association of cells with the ferric oxyhydroxide. Given that a substantial number of cells can remain suspended in the water column, diffusive distribution of organic matter into the upper water column following cell lysis may have facilitated anaerobic respiration, while the ferric oxyhydroxide sedimented to the seafloor. Second, physical processes such as resuspension via density currents (e.g., Krapež et al., 2003; Pickard et al., 2004) could have acted on the Fe-rich precursor sediments, leading to the segregation of the Fe(III) and organic components. Third, during deposition and accumulation at the seafloor, some biomass would have been converted through fermentation and hydrolysis into simpler compounds, such as amino acids, short-chain fatty acids (e.g., lactate and acetate) and H_2 (Rico et al., 2023). A fraction of the fermentation products could have diffused away from the immediate environment, relative to the immobile ferric oxyhydroxide, thereby removing electrons that otherwise would have been available to reduce Fe(III). Indeed, a recent study by Schad et al. (2022) suggested that given realistic sedimentation velocities a dynamic iron cycling likely took place in the water column that involved multiple cycles of Fe(II) oxidation and Fe(III) reduction. It is therefore conceivable that during particle descent, the initial Fe:C ratio changed from 2.8 to an excess of 4.

Implications for Kuruman BIF, Transvaal Supergroup, Kaapvaal Craton, South Africa

Although the experimental findings in this study can be applied to Superior-type BIFs in general, the Kuruman IF is chosen to be discussed in great detail given its significance in BIF research, its available and comprehensive datasets, and importantly, Nic Beukes' fundamental contributions on its origin.

Strong evidence exists in the Kuruman IF that, where preserved, haematite is diagenetically distinct and formed prior to both magnetite and iron-rich carbonate (ankerite and/or siderite). The textures of haematite and magnetite are different, with haematite generally finer grained and flaky to tabular in habit, whereas magnetite, although still very fine grained, has a patchy and anhedral to equidimensional and euhedral habit

(Figure 2A and B). Haematite is also often included in magnetite aggregates (Figure 2B), suggesting the latter post-dates the former. Similar characteristics are observed for some of the iron-rich carbonates as for magnetite, where the carbonates have a different texture to and often includes haematite (Figure 2D). Furthermore, the carbonates have depleted carbon isotopes ($\delta^{13}C_{PDB}$ of -5 to -12 ‰; Kaufman, 1996; Tsikos et al., 2022), suggesting a mixed marine ($\delta^{13}C_{PDB}$ of ~0‰; Faure, 1986) and organic carbon ($\delta^{13}C_{PDB}$ of -30 to -20‰; Freeman, 2001) input. Such iron-rich, ^{13}C-depleted carbonates in IFs have been interpreted to form from a diagenetic redox reaction between ferric oxyhydroxide precipitates and organic carbon, i.e., DIR (e.g., Heimann et al., 2010; Smith et al., 2013; 2023; Smith and Beukes, 2023). The same mechanism has also been inferred for manganese-enriched carbonates that show similar $\delta^{13}C_{PDB}$ values in BIFs (e.g., Johnson et al., 2013; Mhlanga et al., 2023). It should be noted that metamorphic effects (e.g., Kaufman, 1996) could have contributed to the depleted ^{13}C signature in some studied sections, meaning that not all of the carbonates can be accounted for by DIR (e.g., Thompson et al., 2019). In fact, some believe that the $\delta^{13}C_{PDB}$ values were caused by abiological and kinetic effects (Tsikos et al., 2022). However, the latter study showed a similar range of $\delta^{13}C_{PDB}$ that have been mostly interpreted to be of mixed primary and diagenetic origin with both organic DIR and marine carbon input in Palaeoproterozoic BIFs (e.g., Kaufman et al., 1990; Heimann et al., 2010; Johnson et al. 2013; Mhlanga et al., 2023). Therefore, the implication is that magnetite, and likely some of the iron-rich carbonates, had Fe(III) precursors, and that there was significant organic carbon input. The above view is supported by the growth experiments conducted in this study. Where cyanobacteria were co-cultured with Fe(II) and dissolved silica under initially anoxic conditions, the oxygen produced solely via photosynthesis fully oxidised Fe(II) to exclusively form ferrihydrite. Subsequently, precipitated ferrihydrite and cyanobacteria cells flocculated together as mineral-cell aggregates that yielded Fe:C_{org} ratios below 2.8 (except for one extreme case). As discussed above, a ratio below 2.8 strongly implies that there was significant amount of biomass deposited (cyanobacteria cells in this case) along with ferrihydrite, which was then ultimately transformed to Fe(III) mineral phases observed in the Kuruman IF, with little to no secondary alteration.

The iron isotope geochemistry of the Kuruman IF also indicates Fe(II) oxidation as an important process in IF deposition. The commonly accepted mechanisms that fractionate iron isotopes are oxidation (preferentially incorporate ^{56}Fe) and reduction (preferentially incorporates ^{54}Fe) (Welch et al., 2003; Johnson et al., 2008b; Planavsky et al., 2009). Assuming incomplete oxidation of a ferrous iron pool in an oceanic setting with an approximate oceanic crust signature ($\delta^{56}Fe$ close to 0‰), ^{56}Fe would be preferentially incorporated, leading to higher $\delta^{56}Fe$ values (Planavsky et al., 2009). Incomplete diagenetic reduction of the ferric iron (i.e., DIR) would preferentially mobilize ^{54}Fe, with the latter then incorporated into iron-rich carbonates that have lower $\delta^{56}Fe$ values (Johnson et al., 2008b). This is exactly the pattern observed in the Kuruman IF (Johnson et al., 2003; Heimann et al. 2010), indicating that initial oxidation of ferrous iron was an important depositional mechanism.

With regards to geohydrological modelling, if it is assumed that all IFs are a product of non-redox greenalite or carbonate precipitation (Rasmussen et al., 2021), then the heterogenous mineralogical facies and average iron oxidation state of $Fe^{+2.4}$ (Klein and Beukes, 1992; Johnson et al., 2003) must all be the product of secondary alteration processes. Such processes would require oxidising fluids to at least form the observed haematite and magnetite. However, geohydrological modelling conducted by Robbins et al. (2019) on the Hamersley Basin, which shows a strong litho- and sequence stratigraphic correlation to the Griqualand West Basin (Beukes, 1984; Cheney, 1996; Beukes and Guzmer, 2008), indicated that it was highly unlikely (<9% of simulations with unrealistic parameters) that such fluids could cause the observed mineralogy on a basin-wide scale within 2.5 billion years. This further indicates iron oxidation was a significant process in the deposition of the Kuruman IF.

The depositional age constraints allowed for estimates on the compacted rock accumulation rate. Specifically the lower Kuruman BIF was deposited on the shallow continental shelf at a compacted rate of 0.004 to 0.005 mm $year^{-1}$ (Beukes and Gutzmer, 2008). This result is supported by two more recent studies in the Kuruman BIF:

- a predicted range from 0.0036 mm $year^{-1}$ to 0.027 mm $year^{-1}$ based on Co accumulation rate and $\delta^{56}Fe$ exponential responses from three BIF drill cores from the Neoarchaean Transvaal Supergroup in South Africa (Thibon et al., 2019); and
- an average rate of 0.01 mm $year^{-1}$ based on U-Pb dating from early Palaeoproterozoic Kuruman Formation in the Griqualand West basin in South Africa (Lantink et al., 2019).

Given all estimates, the compacted rock accumulation rate ranges from 0.004 to 0.027 mm $year^{-1}$. To put these into more understandable rates, using compaction estimates of 95% (Trendall and Blockley, 1970), the 0.027 mm $year^{-1}$ translates into an unconsolidated deposition rate of ferrihydrite as fast as 0.5 mm $year^{-1}$.

To compare our experimental results with well-established rock records described above, the amount of compacted sediment deposited on an annual basis that was expected to be preserved after DIR was also calculated. The amount of total Fe lost per unit time from each of the 14 experiments at pH 7 and 8 was converted to an estimate of sediment deposition rate using the molar mass (107 g mol^{-1}; Schad et al., 2019b), density of porous ferrihydrite aggregates (2.0 g cm^{-3}; Posth et al., 2010), a sediment compaction ratio (95%; Trendall and Blockley, 1970), and a preservation ratio after DIR in the presence of high dissolved Si concentration (15 to 40%; Schad 2022). The results ranged from 0.0018 to 0.1770 mm $year^{-1}$ when the preservation ratio is 15% and 0.0047 to 0.4719 mm $year^{-1}$ when the preservation ratio is 40%. These estimates incorporate almost the entire range of previous studies. Using the combined range of BIF sedimentation rate from the Kuruman BIF, the initial Fe(II) concentrations required to fulfill the compacted rock accumulation rate in the Kuruman BIF would be from 47 μM

to 212 μM (at pH 7) or from 27 μM to 111 μM (at pH 8), if no other factors are taken into consideration (e.g., turbulent mixing, temperature and pressure changes during deposition). Encouragingly, these predicted Fe(II) concentrations fall within previous estimates of Holland (1984) for the lower limit of 30 μM as dictated by equilibrium with siderite and calcite, and the upper limit of 500 μM based on a conservative estimate of the iron in upwelling hydrothermal fluids (Morris, 1993). It also falls well below the Fe(II) concentrations required for aggregates to settle fast enough to be deposited on continental shelves (see Section reference 4), suggesting that there were more primary sediments produced in the upper water column than the amount that was required to achieve the observed rock accumulation rate. In other words, some primary sediments must have been removed during deposition through the water column. This was possibly a result of combined factors of current transport and higher Fe(III) reduction ratio via DIR. Indeed, previous back-of-the-envelope calculations have suggested that as much as 70% of the ferrihydrite generated in the upper water column would have been reduced via DIR during sedimentation and/or at the seafloor (Konhauser et al., 2005). Most recently, Schad et al. (2022) conducted Fe cycling experiments with both marine phototrophic Fe(II)-oxidising bacteria and DIR bacteria and confirmed that a significant fraction of ferrihydrite was reduced and that organic carbon was liberated from the aggregates. Lastly, our calculation here implies that there was a Fe(II) gradient when the Kuruman BIF formed, i.e., that there were higher Fe(II) concentrations and thus higher sedimentation velocities and rock accumulation rates at the basin-side of BIF deposition, and likely lower concentrations on the inner continental shelf. This interpretation is supported by the stratigraphic section of the Kuruman BIF depicted by Beukes and Gutzmer (2008).

Conclusion

Superior-type BIFs have been routinely studied as a geochemical proxy for Archaean-Palaeoproterozoic seawater geochemistry. Yet, many sedimentary aspects of BIFs, such as depositional environments and sedimentation processes remain poorly resolved. Here, we attempted to simulate ancient seawater geochemistry and recapitulate the initiation of sedimentation processes of BIF sediments, cyanobacteria-ferrihydrite aggregates.

Using a new approach, we assessed the sedimentation velocities of primary BIF sediments across a realistic range of pH values and initial Fe(II) concentrations. Taking essential factors including sedimentation velocity based on laboratory experiments and rock record, Fe(III) accumulation rates, and the residence time of sediments on continental shelves into consideration, it was concluded that BIFs could not have been formed in seawater at pH 6 or less due to insufficient sedimentation velocity. Instead, they were most likely deposited in an ocean at pH 7 or higher. The $Fe:C_{org}$ ratios in the sediments formed during oxygenic photosynthesis under a closed atmosphere were mostly below the experimental threshold of 2.8, which undermines the prerequisite for BIF formation, i.e., excess Fe(III) in the primary sediments. This contradiction implies that there were mechanisms that separated the biomass from Fe(III) minerals after aggregate formation but before magnetite (and siderite) formation during diagenesis. However, both encrusted and shielded cell biomass in the aggregates would have been unavailable for heterotrophic consumption and, therefore, a small percentage of organic carbon was preserved in Superior-type BIF.

Simulation of ancient oceans in laboratory settings is inherently challenging whether it is placed in the context of geochemistry or fluid dynamics. The sedimentation experiments aimed to gain insight into *in situ* cell-mineral aggregation behavior in still water, by measuring maximum and average sedimentation speeds under varying pH and initial Fe(II) levels, to build upon existing BIF sedimentation research. Although our experimental results matched coherently with estimates from existing rock records, especially with the Kuruman BIF in South Africa, it should be noted that our experiments were also limited by the experimental conditions. In particular, the effects of turbulent mixing on sedimentation velocity of coagulated aggregates on continental shelves; the possible different sedimentation behaviours with other Fe(II)-oxidising bacteria under similar geochemical conditions as in this study; and effect of presence/absence of abundant dissolved oxygen on the sedimentation behaviour and velocities. These issues will be taken into consideration in future similar multi-disciplinary studies.

Acknowledgements

This work was supported by NSERC Discovery Grants to KOK (RGPIN-2020-05189), BRS, MKG (RGPIN-2020-05138), GWO (RGPIN-2016-05448), LJR (RGPIN-2021-02523) and DSA (RGPIN-2020-05289). Andreas Kappler acknowledges support by the German Research Foundation (DFG) under Germany's Excellence Strategy (Cluster of Excellence EXC2124, project ID 390838134) and by project KA 1736/65-1. Iñaki Yusta and Javier Sánchez España acknowledge funding sources by the Spanish Ministry of Economy, Industry and Competitiveness through the National Research Agency (FEDER funds, Grant CGL2016-74984-R) and by Basque Government grant (Consolidated Group IT1678-22). We acknowledge the support of the personnel at the SGIker facilities in the UPV/EHU for the XRD and SEM work (Javier Sangüesa). We would like to thank Jens Gutzmer, Harilaos Tsikos, and an anonymous reviewer for their constructive comments on this work.

References

Anbar, A.D., Duan, Y., Lyons, T.W., Arnold, G.L., Kendall, B., Creaser, R.A., Kaufman, A.J., Gordon, G.W., Scott, C., Garvin, J. and Buick, R., 2007. A whiff of oxygen before the great oxidation event? Science, 317, 1903-1906.

Baldwin, W.W., Myer, R., Anderson, E. and Koch, A.L., 1995. Buoyant density of Escherichia coli is determined solely by the osmolarity of the culture medium. Archives of Microbiology, 164, 155-157.

Bau, M. and Dulski, P., 1996. Distribution of yttrium and rare-earth elements in the Penge and Kuruman iron-formations, Transvaal Supergroup. South Africa. Precambrian Research, 79, 37-55.

Baur, M.E., Hayes, J.M., Studley, S.A. and Walter, M.R., 1985. Millimeter-scale variations of stable isotope abundances in carbonates from banded iron-formations in the Hamersley Group of Western Australia. Economic Geology, 80, 270-282.

Bekker, A., Holland, H.D., Wang, P.L., Rumble Iii, D., Stein, H.J., Hannah, J.L., Coetzee, L.L. and Beukes, N.J., 2004. Dating the rise of atmospheric oxygen. Nature, 427, 117-120.

Bekker, A., Slack, J.F., Planavsky, N., Krapez, B., Hofmann, A., Konhauser, K.O. and Rouxel, O.J. 2010. Iron formation: the sedimentary product of a complex interplay among mantle, tectonic, oceanic, and biospheric processes. Economic Geology, 105, 467-508.

Beukes, N.J., 1980. Lithofacies and stratigraphy of the Kuruman and Griquatown iron-formations, northern Cape Province, South Africa. South African Journal of Geology, 83, 69-86.

Beukes, N. J., 1983 Palaeoenvironmental setting of iron-formations in the depositional basin of the Transvaal Supergroup, South Africa. In: A.F. Trendall and R.C. Morris (Editors), Iron-formation: Facts and Problems. Developments in Precambrian Geology, 6, 131-209.

Beukes, N.J., 1984. Sedimentology of the Kuruman and Griquatown iron-formations, Transvaal Supergroup, Griqualand West, South Africa. Precambrian Research, 24, 47-84.

Beukes, N.J., 1987. Facies relations, depositional environments and diagenesis in a major early Proterozoic stromatolitic carbonate platform to basinal sequence, Campbellrand Subgroup, Transvaal Supergroup, southern Africa. Sedimentary Geology, 54, 1-46.

Beukes, N.J. and Gutzmer, J., 2008. Origin and paleoenvironmental significance of major iron formations at the Archaean-Palaeoproterozoic boundary. In: S. Hagemann, C.A. Rosière, J. Gutzmer and N.J. Beukes (Editors) Banded Iron Formation-Related High-Grade Iron Ore. Society of Economic Geologists, Reviews in Economic Geology, 15, 5-47.

Blättler, C.L., Kump, L.R., Fischer, W.W., Paris, G., Kasbohm, J.J. and Higgins, J.A., 2017. Constraints on ocean carbonate chemistry and pCO_2 in the Archaean and Palaeoproterozoic. Nature Geoscience, 10, 41-45.

Bray, D.F., Bagu, J. and Koegler, P., 1993. Comparison of hexamethyldisilazane (HMDS), Peldri II, and critical-point drying methods for scanning electron microscopy of biological specimens. Microscopy Research and Technique, 26, 489-495.

Cheney, E.S., 1996. Sequence stratigraphy and plate tectonic significance of the Transvaal succession of southern Africa and its equivalent in Western Australia. Precambrian Research, 79, 3-24.

Craddock, P.R. and Dauphas, N., 2011. Iron and carbon isotope evidence for microbial iron respiration throughout the Archaean. Earth and Planetary Science Letters, 303, 121-132.

Defne, Z. and Ganju, N.K., 2015. Quantifying the residence time and flushing characteristics of a shallow, back-barrier estuary: Application of hydrodynamic and particle tracking models. Estuaries and Coasts, 38, 1719-1734.

Drits, V.A., Sakharov, B.A., Salyn, A.L. and Manceau, A., 1993. Structural model for ferrihydrite. Clay Minerals, 28, 185-207.

Dzombak, D.A. and Morel, F.M.M., 1990. Surface Complexation Modeling: Hydrous Ferric Oxide. New Jersey, USA, John Wiley & Sons, Ltd.

Edmond, J.M., Von Damm, K.L., McDuff, R.E. and Measures, C.I., 1982. Chemistry of hot springs on the East Pacific Rise and their effluent dispersal. Nature, 297, 187-191.

Faure, G., 1986. Principles of isotope geology. Wiley, New York, 589.

Fischer, W.W. and Knoll, A.H., 2009. An iron shuttle for deepwater silica in Late Archaean and early Palaeoproterozoic iron formation. Geological Society of America Bulletin, 121, 222-235.

Freeman, K.H., 2001. Isotopic biogeochemistry of marine organic carbon. Reviews Mineralogy and Geochemistry, 43, 579-605.

Frost, C.D., von Blanckenburg, F., Schoenberg, R., Frost, B.R. and Swapp, S.M., 2007. Preservation of Fe isotope heterogeneities during diagenesis and metamorphism of banded iron formation. Contributions to Mineralogy and Petrology, 153, 211.

Gole, M.J. and Klein, C., 1981. Banded iron-formations through much of Precambrian time. The Journal of Geology, 89, 69-183.

Grotzinger, J.P. and Kasting, J.F., 1993. New constraints on Precambrian Ocean composition. The Journal of Geology, 101, 235-243.

Gutzmer, J., Chisonga, B.C., Beukes, N.J. and Mukhopadhyay, J., 2008. The geochemistry of banded iron formation-hosted high-grade haematite-martite iron ores. In: S. Hagemann, C.A. Rosière, J. Gutzmer and N.J. Beukes (Editors), Banded Iron Formation-Related High-Grade Iron Ore. Society of Economic Geologists, Reviews in Economic Geology, 15, 5-47.

Gumsley, A.P., Chamberlain, K.R., Bleeker, W., Söderlund, U., de Kock, M.O., Larsson, E.R. and Bekker, A., 2017. Timing and tempo of the Great Oxidation Event. Proceedings of the National Academy of Sciences, 114, 1811-1816.

Halama, M., Swanner, E.D., Konhauser, K.O. and Kappler, A., 2016. Evaluation of siderite and magnetite formation in BIFs by pressure-temperature experiments of Fe(III) minerals and microbial biomass. Earth and Planetary Science Letters, 450, 243-253.

Halevy, I. and Bachan, A., 2017. The geologic history of seawater pH. Science, 355, 1069-1071.

Hegler, F., Posth, N.R., Jiang, J. and Kappler, A., 2008. Physiology of phototrophic iron (II)-oxidising bacteria: implications for modern and ancient environments. FEMS Microbiology Ecology, 66, 250-260.

Heimann, A., Johnson, C.M., Beard, B.L., Valley, J.W., Roden, E.E., Spicuzza, M.J. and Beukes, N.J., 2010. Fe, C, and O isotope compositions of banded iron formation carbonates demonstrate a major role for dissimilatory iron reduction in~ 2.5 Ga marine environments. Earth and Planetary Science Letters, 294, 8-18.

Holland, H.D., 1973. The oceans; A possible source of iron in iron-formations. Economic Geology, 68, 1169-1172.

Holland, H.D., 1984. The chemical evolution of the atmosphere and oceans. Lawrenceville, New Jersey, Princeton University Press. 337-428.

James, H.L., 1954. Sedimentary facies of iron-formation. Economic Geology, 49, 235-293.

Johnson, C.M., Beard, B.L., Beukes, N.J., Klein, C. and O'Leary, J.M., 2003. Ancient geochemical cycling in the Earth as inferred from Fe isotope studies of banded iron formations from the Transvaal Craton. Contributions to Mineralogy and Petrology, 144, 523-547.

Johnson, C.M., Beard, B.L. and Roden, E.E., 2008a. The iron isotope fingerprints of redox and biogeochemical cycling in modern and ancient Earth. Annual Review of Earth and Planetary Sciences, 36, 457-493.

Johnson, C.M., Beard, B.L., Klein, C., Beukes, N.J. and Roden, E.E., 2008b. Iron isotopes constrain biologic and abiologic processes in banded iron formation genesis. Geochimica et Cosmochimica Acta, 72, 151-169.

Johnson, C.M., Ludois, J.M., Beard, B.L., Beukes, N.J. and Heimann, A., 2013. Iron formation carbonates: Paleoceanographic proxy or recorder of microbial diagenesis? Geology, 41, 1147-1150.

Kappler, A. and Newman, D.K., 2004. Formation of Fe (III)-minerals by Fe (II)-oxidising photoautotrophic bacteria. Geochimica et Cosmochimica Acta, 68, 1217-1226.

Kappler, A., Pasquero, C., Konhauser, K.O. and Newman, D.K., 2005. Deposition of banded iron formations by anoxygenic phototrophic Fe (II)-oxidising bacteria. Geology, 33, 865-868.

Kaufman, A.J., 1996. Geochemical and mineralogic effects of contact metamorphism on banded iron-formation: an example from the Transvaal Basin, South Africa. Precambrian Research, 79, 171-194.

Kaufman, A.J., Hayes, J.M. and Klein, C., 1990. Primary and diagenetic controls of isotopic compositions of iron-formation carbonates. Geochimica et Cosmochimica Acta, 54, 3461-3473.

Keller, D.S., Tassara, S., Robbins, L.J., Lee, C-T.A., Ague, J.J. and Dasgupta, R., 2023. Links between large igneous province volcanism and subducted iron formations. Nature Geoscience, 16, 527-533.

Kenov, I.A., Garcia, A.C. and Neves, R., 2012. Residence time of water in the Mondego estuary (Portugal). Estuarine, Coastal and Shelf Science, 106, 13-22.

Khouchaf, L., Boulahya, K., Das, P.P., Nicolopoulos, S., Kis, V.K. and Lábár, J.L., 2020. Study of the microstructure of amorphous silica nanostructures using high-resolution electron microscopy, electron energy loss spectroscopy, X-ray powder diffraction, and electron pair distribution function. Materials, 13, 4393.

Kleber, M., Mikutta, R., Torn, M.S. and Jahn, R., 2005. Poorly crystalline mineral phases protect organic matter in acid subsoil horizons. European Journal of Soil Science, 56, 717-725.

Klein, C., 2005. Some Precambrian banded iron-formations (BIFs) from around the world: Their age, geologic setting, mineralogy, metamorphism, geochemistry, and origin. American Mineralogist, 90, 1473-1499.

Klein, C. and Beukes, N.J., 1989. Geochemistry and sedimentology of a facies

transition from limestone to iron-formation deposition in the Early Proterozoic Transvaal Supergroup, South Africa. Economic Geology, 84, 1733-1774.

Klein C. and Beukes N.J., 1992. Proterozoic iron-formations. In: K.C. Condie (Editor), Proterozoic crustal evolution. Elsevier, Amsterdam, 383-418.

Köhler, I., Konhauser, K.O., Papineau, D., Bekker, A. and Kappler, A., 2013. Biological carbon precursor to diagenetic siderite with spherical structures in iron formations. Nature Communications, 4, 1-7.

Konhauser, K.O., Hamade, T., Morris, R.C., Ferris, F.G., Southam, G., Raiswell, R. and Canfield, D.E., 2002. Could bacteria have formed the Precambrian banded iron formations? Geology, 30, 1079-1082.

Konhauser, K.O., Newman, D.K. and Kappler, A., 2005. The potential significance of microbial Fe (III) reduction during deposition of Precambrian banded iron formations. Geobiology, 3, 167-177.

Konhauser, K.O., Lalonde, S.V., Planavsky, N., Pecoits, E., Lyons, T., Mojzsis, S., Rouxel, O.J., Barley, M., Rosiere, C., Fralick, P.W., Kump, L.R. and Bekker, A., 2011. Chromium enrichment in iron formations record Earth's first acid rock drainage during the Great Oxidation Event. Nature, 478, 369-373.

Konhauser, K.O., Planavsky, N.J., Hardisty, D.S., Robbins, L.J., Warchola, T.J., Haugaard, R., Lalonde, S.V., Partin, C.A., Oonk, P.B.H., Tsikos, H. and Lyons, T.W., 2017. Iron formations: A global record of Neoarchaean to Palaeoproterozoic environmental history. Earth-Science Reviews, 172, 140-177.

Konhauser, K.O., Robbins, L.J., Alessi, D.S., Flynn, S.L., Gingras, M.K., Martinez, R.E., Kappler, A., Swanner, E.D., Li, Y-L., Crowe, S.A., Planavsky, N.J., Reinhard, C.T. and Lalonde, S.V., 2018. Phytoplankton contributions to the trace-element composition of Precambrian banded iron formations. Geological Society of America Bulletin, 130, 941-951.

Konhauser, K.O., Kappler, A., Lalonde, S.V. and Robbins, L.J., 2023. Trace elements in iron formation as a window into biogeochemical evolution accompanying the oxygenation of Earth's atmosphere. Geoscience Canada, 50, 239-258.

Krapež, B., Barley, M.E. and Pickard, A.L., 2003. Hydrothermal and resedimented origins of the precursor sediments to banded iron formation: sedimentological evidence from the Early Palaeoproterozoic Brockman Supersequence of Western Australia. Sedimentology, 50, 979-1011.

Krissansen-Totton, J., Arney, G.N. and Catling, D.C., 2018. Constraining the climate and ocean pH of the early Earth with a geological carbon cycle model. Proceedings of the National Academy of Sciences USA, 115, 4105-4110.

Lalonde, K., Mucci, A., Ouellet, A. and Gélinas, Y., 2012. Preservation of organic matter in sediments promoted by iron. Nature, 483, 198-200.

Lantink, M.L., Davies, J.H., Mason, P.R., Schaltegger, U. and Hilgen, F.J., 2019. Climate control on banded iron formations linked to orbital eccentricity. Nature Geoscience, 12, 369-374.

Li, W., Czaja, A.D., Van Kranendonk, M.J., Beard, B.L., Roden, E.E. and Johnson, C.M., 2013. An anoxic, Fe (II)-rich, U-poor ocean 3.46 billion years ago. Geochimica et Cosmochimica Acta, 120, 65-79.

Li, Y-L., Konhauser, K.O., Kappler, A. and Hao, X-L., 2013. Experimental low-grade alteration of biogenic magnetite indicates microbial involvement in generation of banded iron formations. Earth and Planetary Science Letters, 36, 229-237.

Li, Y., Sutherland, B.R., Gingras, M.K., Owttrim, G.W. and Konhauser, K.O., 2021. A novel approach to investigate the deposition of (bio) chemical sediments: The sedimentation velocity of cyanobacteria–ferrihydrite aggregates. Journal of Sedimentary Research, 91, 390-398.

Lyons, T.W., Reinhard, C.T. and Planavsky, N.J., 2014. The rise of oxygen in Earth's early ocean and atmosphere. Nature, 506, 307-315.

Maliva, R.G., Knoll, A.H. and Siever, R., 1989. Secular change in chert distribution; a reflection of evolving biological participation in the silica cycle. Palaios, 4, 519-532.

Martinez, R. E., Konhauser, K. O., Paunova, N., Alessi, D. S. and Kappler, A., 2016. Surface reactivity of the anaerobic photoferrotrophic bacterium *Rhodovulvum iodosum*: implications for trace metal budgets in ancient oceans and banded iron formations. Chemical Geology, 442, 113-120.

Mhlanga, X.R., Tsikos, H., Lee, B., Rouxel, O.J., Boyce, A.C., Harris, C. and Lyons, T.W. 2023., The Palaeoproterozoic Hotazel BIF-Mn Formation as an archive of Earth's earliest oxygenation. Earth-Science Reviews, 240, 104389.

Morris, R.C., 1993. Genetic modelling for banded iron-formation of the Hamersley Group, Pilbara Craton, Western Australia. Precambrian Research, 60, 243-286.

Oonk, P.B.H., Tsikos, H., Mason, P.R.D., Henkel, S., Staubwasser, M., Fryer, L., Poulton, S.W. and Williams, H.M., 2017. Fraction-specific controls on the trace element distribution in iron formations: Implications for trace metal stable isotope proxies. Chemical Geology, 474, 17-32.

Pavlov, A.A. and Kasting, J.F., 2002. Mass-independent fractionation of sulfur isotopes in Archaean sediments: strong evidence for an anoxic Archaean atmosphere. Astrobiology, 2, 27-41.

Pecoits, E., Gingras, M.K., Barley, M.E., Kappler, A., Posth, N.R. and Konhauser, K.O., 2009. Petrography and geochemistry of the Dales Gorge banded iron formation: Paragenetic sequence, source and implications for palaeo-ocean chemistry. Precambrian Research, 172, 163-187.

Perry, E.C., Tan, F.C. and Morey, G.B., 1973. Geology and stable isotope geochemistry of the Biwabik Iron Formation, northern Minnesota. Economic Geology, 68, 1110-1125.

Pickard, A.L., 2002. SHRIMP U-Pb zircon ages of tuffaceous mudrocks in the Brockman Iron Formation of the Hamersley Range, Western Australia. Australian Journal of Earth Sciences, 49, 491-507.

Pickard, A.L., Barley, M.E. and Krapež, B., 2004. Deep-marine depositional setting of banded iron formation: sedimentological evidence from interbedded clastic sedimentary rocks in the early Palaeoproterozoic Dales Gorge Member of Western Australia. Sedimentary Geology, 170, 37-62.

Posth, N.R., Huelin, S., Konhauser, K.O. and Kappler, A., 2010. Size, density and composition of cell–mineral aggregates formed during anoxygenic phototrophic Fe (II) oxidation: impact on modern and ancient environments. Geochimica et Cosmochimica Acta, 74, 3476-3493.

Posth, N.R., Konhauser, K.O. and Kappler, A., 2013. Microbiological processes in banded iron formation deposition. Sedimentology, 60, 1733-1754.

Planavsky, N., Rouxel, O., Bekker, A., Shapiro, R., Fralick, P. and Knudsen, A., 2009. Iron-oxidising microbial ecosystems thrived in late Palaeoproterozoic redox-stratified oceans. Earth and Planetary Science Letters, 286, 230-242.

Planavsky, N., Rouxel, O.J., Bekker, A., Hofmann, A., Little, C.T. and Lyons, T.W., 2012. Iron isotope composition of some Archaean and Proterozoic iron formations. Geochimica et Cosmochimica Acta, 80, 158-169.

Planavsky, N.J., Reinhard, C.T., Wang, X., Thomson, D., McGoldrick, P., Rainbird, R.H., Johnson, T., Fischer, W.W. and Lyons, T.W., 2014. Low Mid-Proterozoic atmospheric oxygen levels and the delayed rise of animals. Science, 346, 635-638.

Poulton, S.W., Bekker, A., Cumming, V.M., Zerkle, A.L., Canfield, D.E. and Johnston, D.T., 2021. A 200-million-year delay in permanent atmospheric oxygenation. Nature, 592, 232-236.

Rasmussen, B., Muhling, J.R. and Krapež, B., 2021. Greenalite and its role in the genesis of early Precambrian iron formations – A review. Earth-Science Reviews, 217, 103613.

Rico, K., Schad, M., Picard, A., Kappler, A., Konhauser, K.O. and Mahmoudi, N., 2023. Resolving the fate of trace metals during microbial remineralization of phytoplankton biomass in precursor banded iron formation sediments. Earth and Planetary Science Letters, 607, 118068.

Robbins, L.J., Funk S.P., Flynn, S.L., Warchola, T.J., Li, Z., Lalonde, S.V., Rostron, B.J., Smith, A.J.B., Beukes, N.J., De Kock, M.O., Heaman, L.M., Alessi, D.S. and Konhauser, K.O., 2019. Hydrogeological constraints on the formation of Palaeoproterozoic banded iron formations. Nature Geoscience, 12, 558-563.

Roden, E.E. and Zachara, J.M., 1996. Microbial reduction of crystalline iron (III) oxides: influence of oxide surface area and potential for cell growth. Environmental Science & Technology, 30, 618-1628.

Schad, M., Konhauser, K.O., Sánchez-Baracaldo, P., Kappler, A. and Bryce, C., 2019a. How did the evolution of oxygenic photosynthesis influence the temporal and spatial development of the microbial iron cycle on ancient Earth? Free Radical Biology and Medicine, 140, 154-166.

Schad, M., Halama, M., Bishop, B., Konhauser, K.O. and Kappler, A., 2019b. Temperature fluctuations in the Archaean ocean as trigger for varve-like deposition of iron and silica minerals in banded iron formation. Geochimica et Cosmochimica Acta, 265, 386-412.

Schad, M., Byrne, J.M., ThomasArrigo, L.K., Kretzschmar, R., Konhauser, K.O. and Kappler, A., 2022. Microbial Fe cycling in a simulated Precambrian Ocean environment: Implications for secondary mineral (trans) formation

and deposition during BIF genesis. Geochimica et Cosmochimica Acta, 331, 165-191.

Schröder, S., Bedorf, D., Beukes, N.J. and Gutzmer, J., 2011. From BIF to red beds: Sedimentology and sequence stratigraphy of the Palaeoproterozoic Koegas Subgroup (South Africa). Sedimentary Geology, 236, 25-44.

Schumacher, B.A., 2002. Methods for the determination of total organic carbon (TOC) in soils and sediments. Doctoral dissertation thesis. Las Vegas, United States Environmental Protection Agency, Environmental Sciences Division National Exposure Research Laboratory. 1-23.

Schwertmann, U.T. and Fischer, W.R., 1973. Natural "amorphous" ferric hydroxide. Geoderma, 10, 237-247.

Siahi, M., Tsikos, H., Rafusa, S., Oonk, P.B.H., Mhlanga, X.R., van Niekerk, D., Mason, P.R.D. and Harris, C., 2020. Insights into the processes and controls on the absolute abundance and distribution of manganese in Precambrian iron formations. Precambrian Research, 350, 105878.

Siever, R., 1992. The silica cycle in the Precambrian. Geochimica et Cosmochimica Acta, 56, 3265-3272.

Singer, P.C. and Stumm, W., 1970. Acidic mine drainage: the rate-determining step. Science, 167, 1121-1123.

Smith, A.J.B., 2018. The iron formations of Southern Africa. In: S. Siegesmund, M.A.S. Basei, P. Oyhantçabal and S. Oriolo (Editors), Geology of Southwest Gondwana. Springer, Cham, 469-491.

Smith, A.J.B. and Beukes, N.J., 2016. Palaeoproterozoic banded iron formation-hosted high-grade haematite iron ore deposits of the Transvaal Supergroup, South Africa. Episodes, 39, 269-284.

Smith, A.J.B. and Beukes, N.J., 2023. The paleoenvironmental implications of pre-Great Oxidation Event manganese deposition in the Mesoarchaean Ijzermijn Iron Formation Bed, Mozaan Group, Pongola Supergroup, South Africa. Precambrian Research, 384, 106922.

Smith, A.J.B., Beukes, N.J. and Gutzmer, J., 2013. The composition and depositional Environments of Mesoarchaean iron formations of the West Rand Group of the Witwatersrand Supergroup, South Africa. Economic Geology, 108, 111-134.

Smith, A.J.B., Beukes, N.J., Cochrane, J.M. and Gutzmer, J., 2023. Manganese carbonate-bearing mudstone of the Witwatersrand-Mozaan succession in southern Africa as evidence for bacterial manganese respiration and availability of free molecular oxygen in Mesoarchaean oceans. South African Journal of Geology, 126, 29-48.

Steinhoefel, G., von Blanckenburg, F., Horn, I., Konhauser, K.O., Beukes, N.J. and Gutzmer, J. 2010. Deciphering formation processes of banded iron formations from the Transvaal and the Hamersley successions by combined Si and Fe isotope analysis using UV femtosecond laser ablation. Geochimica et Cosmochimica Acta, 74, 2677-2696.

Stookey, L.L., 1970. Ferrozine-a new spectrophotometric reagent for iron. Analytical Chemistry, 42, 779-781.

Stumm, W. and Morgan, J.J., 2012. Aquatic chemistry: chemical equilibria and rates in natural waters. New Jersey, John Wiley & Sons, 61-63.

Sutherland, B.R., Barrett, K.J. and Gingras, M.K., 2015. Clay settling in fresh and salt water. Environmental Fluid Mechanics, 15, 47-160.

Swanner, E.D., Wu, W., Hao, L., Wüstner, M.L., Obst, M., Moran, D.M., McIlvin, M.R., Saito, M.A. and Kappler, A., 2015. Physiology, Fe (II) oxidation, and Fe mineral formation by a marine planktonic cyanobacterium grown under ferruginous conditions. Frontiers in Earth Science, 3, 60.

Thibon, F., Blichert-Toft, J., Tsikos, H., Foden, J., Albalat, E. and Albarede, F., 2019. Dynamics of oceanic iron prior to the Great Oxygenation Event. Earth and Planetary Science Letters, 506, 360-370.

Thompson, K.J., Kenward, P.A., Bauer, K.W., Warchola, T., Gauger, T., Martinez, R., Simister, R.L., Michiels, C.C., Llirós, M., Reinhard, C.T. and Kappler, A., 2019. Photoferrotrophy, deposition of banded iron formations, and methane production in Archaean oceans. Science Advances, 5, eaav2869.

Tosca, N.J., Guggenheim, S. and Pufahl, P.K., 2016. An authigenic origin for Precambrian greenalite: Implications for iron formation and the chemistry of ancient seawater. Geological Society of America Bulletin, 128, 511-530.

Trendall, A.F. and Blockley, J.G., 1970, The iron-formations of the Precambrian Hamersley Group, Western Australia: Geological Survey of Western Australia Bulletin, 119, 366.

Turner, J.S., 1973. Buoyant Convection from Isolated Sources, In: G.K. Batchelor and J.W. Miles (Editors), Buoyancy Effects in Fluid. Cambridge University Press, 165-206.

Tsikos, H., Siahi, M., Rafuza, S., Mhlanga, X.R., Oonk, P.B.H., Papadopoulos, V., Boyce, A.J., Mason, P.R.D., Harris, C., Gröcke, D.R. and Lyons, T.W., 2022. Carbon isotope stratigraphy of Precambrian iron formations and possible significance for the early biological pump. Gondwana Research, 2022, 416-428.

Walker, J.C., 1984. Suboxic diagenesis in banded iron formations. Nature, 309, 340-342.

Warke, M.R., Di Rocco, T., Zerkle, A.L., Lepland, A., Prave, A.R., Martin, A.P., Ueno, Y., Condon, D.J. and Claire, M.W., 2020. The great oxidation event preceded a Paleoproterozoic "snowball Earth". Proceedings of the National Academy of Sciences, 117, 13314-13320.

Welch, S.A., Beard, B.L., Johnson, C.M. and Braterman, P.S., 2003. Kinetic and equilibrium Fe isotope fractionation between aqueous Fe(II) and Fe(III). Geochimica et Cosmochimica Acta, 67, 4231-4250.

Wu, W., Swanner, E.D., Hao, L., Zeitvogel, F., Obst, M., Pan, Y. and Kappler, A., 2014. Characterization of the physiology and cell–mineral interactions of the marine anoxygenic phototrophic Fe (II) oxidiser Rhodovulum iodosum–implications for Precambrian Fe(II) oxidation. FEMS Microbiology Ecology, 88, 503-515.

Zhang, S., Li, Y., Leng, W. and Gurnis, M., 2023. Photoferrotrophic bacteria initiated plate tectonics in the Neoarchaean. Geophysical Research Letters, 50, e2023GL103553.

Editorial handling: J. Gutzmer.